Observations of microphysical properties and radiative effects of a contrail cirrus ~~and natural cirrus~~outbreak over the North Atlantic

Ziming Wang[1,2], Luca Bugliaro[1], Tina Jurkat-Witschas[1], Romy Heller[1], Ulrike Burkhardt[1], Helmut Ziereis[1], Georgios Dekoutsidis[1], Martin Wirth[1], Silke Groß[1], Simon Kirschler[1,3], Stefan Kaufmann[1], Christiane Voigt[1,3]

[1]Institute of Atmospheric Physics, German Aerospace Center (DLR), Oberpfaffenhofen, 82234, Germany
[2]Meteorological Institute Munich, Ludwig-Maximilians-Universität München, Munich, 80333, Germany
[2]Institute of Atmospheric Physics, Johannes Gutenberg University, Mainz, 55128, Germany

Correspondence to: Ziming Wang (Ziming.Wang@dlr.de) and Luca Bugliaro (Luca.Bugliaro@dlr.de)

Abstract. Contrail cirrus constitute the largest radiative forcing (RF) component to~~of~~ the total aviation effect on climate. However, the ~~difference of~~ microphysical properties and radiative effects ~~between contrails,~~of contrail cirrus and natural cirrus clouds in the same meteorological conditions are still not completely resolved. Motivated by these uncertainties, we investigate ~~the~~ an extended cirrus region perturbed by aviation in the North Atlantic Region (NAR) on 26 March 2014 during the Mid Latitude Cirrus (ML-CIRRUS) experiment. On that day, high air traffic density in the NAR combined with large scale cold and humid ambient conditions favouring the formation of a contrail cirrus outbreak situation. In addition, low coverage by low-level water clouds and the homogeneous oceanic albedo increase the sensitivity to retrieve cirrus properties and their radiative effect from satellite remote sensing. This allowed to extend current knowledge on contrail cirrus by combining airborne in situ, lidar and satellite observations.

In the synoptic context of a ridge cirrus ~~cloud~~, an extended thin ice cloud with many persistent contrails and contrail cirrus ~~can be~~has been observed for many hours with the geostationary Meteosat Second Generation (MSG)/Spinning Enhanced Visible and InfraRed Imager (SEVIRI) from the early morning hours until dissipation ~~close to 14 UTC~~after noon. Airborne lidar observations aboard the German High Altitude and LOng Range Research Aircraft (HALO) suggest that this ~~cloud is mainly of~~ cirrus has a significant anthropogenic ~~origin~~contribution from aviation. ~~We develop a new method~~ A new method based on in situ measurements was used to ~~to~~ distinguish between contrails, contrail cirrus and natural cirrus based on ~~in situ measurements of~~ ice number and gas phase NO ~~gas~~ concentrations. ~~It turns out~~Results show that the effective radii (R_{eff}) of contrails and contrail cirrus ~~and contrails~~ are ~~in the range of~~between 3 ~~to~~ and 53 µm and are about 18% smaller than ~~that of~~ natural cirrus.~~, hence~~ We find that a difference in R_{eff} between contrail cirrus and natural cirrus survives in this contrail cirrus outbreak event~~is still present~~. ~~Ice particle sizes in contrail cirrus are on average 114% larger than in contrails. The optical thickness of natural cirrus, contrail cirrus and contrails derived from satellite data has similar distributions with average values of 0.21, 0.24 and 0.15 for these three cloud types, respectively.~~ As for radiative effects, a new method to estimate top-of-atmosphere instantaneous RF in the solar and thermal range is developed based on radiative transfer model simulations exploiting in situ and lidar measurements, satellite observations and ERA5 reanalysis data for both cirrus and cirrus-free regions. Broadband irradiances estimated from our simulations compare well with satellite observations from MSG ~~and the Geostationary Earth Radiation Budget (GERB)~~, indicating that our method provides a good representation of the real atmosphere and can thus be used to determine RF of ice clouds ~~probed during this flight~~. ~~Contrails net RF is smaller by a factor of 4 compared to contrail cirrus. On average, the net RF of contrails and contrail cirrus is more strongly warming than that of natural cirrus.~~ For a larger spatial area around the flight path, ~~the RF is well related to that along the flight track.~~ we find that the contrail cirrus outbreak is warming ~~contrail cirrus and cirrus~~ in the early morning and cooling ~~contrail cirrus and cirrus~~ during the day. The methods presented here and the results will be valuable for a future research to constrain uncertainties in the assessment of ~~climate~~ radiative impacts of contrail cirrus and natural cirrus and for the formulation and evaluation of contrail mitigation options.

1 Introduction

Aviation accounts for about 3.5% of global effective radiative forcing (ERF) from all human activities (Lee et al., 2021). Among the individual aviation contributions, contrail cirrus contributes to more than 50% of the total aviation ERF component (Lee et al., 2021). Contrail cirrus and natural cirrus are both high level clouds composed of ice crystals that form and evolve in ice supersaturated regions (ISSRs) (Minnis et al., 2004). Contrails form when the hot and humid jet engine exhaust at cruise levels mixes with the cool ambient atmosphere, which at temperatures lower than the Schmidt-Appleman criterion (Schumann, 1996) can lead to a local liquid saturation of the plume. The emitted soot particles act as condensation nuclei to form liquid droplets that freeze subsequently in the young contrails (Bier et al., 2017; Kärcher and Voigt., 2017; Kärcher, 2018; ~~Kärcher and Voigt., 2018;~~ Kleine et al., 2018). In ISSRs, persistent contrails may grow and spread out to form contrail-induced cirrus (Burkhardt and Kärcher, 2011; Schumann et al., 2017). By reflecting incident solar radiation and trapping upwelling radiation within the Earth's atmosphere, they result in an imbalance of radiation budget in both the shortwave (SW) solar and longwave (LW) ~~solar~~ terrestrial spectrum (Stuber et al., 2006). The net radiative forcing (RF) is positive (Rädel and Shine, 2008; Burkhardt et al., 2018; Gettelman et al., 2021) and RF due to contrail cirrus greatly exceeds that from linear contrails (Burkhardt and Kärcher, 2011; Voigt et al., 2011; Burkhardt et al., 2018). Due to various reasons, feedback of natural clouds, the radiative response to the presence of contrail cirrus, the uncertainty in upper tropospheric water budget (including initial contrail properties, contrail cirrus properties and relative humidity), contrail cirrus schemes (see Lee et al., 2021), and the challenges in measuring and separating contrail cirrus from natural cirrus, a best central estimate of the contrail cirrus RF remains challenging, further limiting projections of aviation climate impact and formulations of mitigation options other than carbon dioxide (CO_2) emissions (Voigt et al., 2021). Knowledge gaps still exist regarding the large variability in the contrail life cycles (Bier et al., 2017), and optical properties which then determine their radiative response to the climate system (Forster et al., 2007; Grewe et al., 2017).

Contrails may form in, overlap, merge, and interact with natural cirrus (Duda et al., 2001; Vázquez-Navarro et al., 2015; Sanz-Morère et al., 2021). Contrail cirrus primarily differs from natural cirrus by their larger ice number concentrations (N) (Heymsfield et al., 2010b; Voigt et al., 2010; Voigt et al., 2017; Sanz-Morère et al., 2020). Consequently, microphysical process rates, which control their life cycle, and radiative effects can be very different to those in natural cirrus and are dependent on soot number emissions (Bier et al., 2017). ~~Besides soot particles emitted from aviation, volatile aerosols inject into the upper troposphere (UT) in ice subsaturated conditions and can alter cirrus clouds and liquid water clouds at a later stage (Hendricks et al., 2005; Lee et al., 2009; Schumann et al. 2015; Urbanek et al., 2018; Righi et al., 2021).~~ Furthermore, natural cirrus locally optically thickens by embedded contrails (Tesche et al., 2016; Quaas et al., 2021; Schumann et al., 2021a, b), but contrails can also cause a decrease in natural cloudiness (Burkhardt and Kärcher, 2011). These aspects are still subject of current research (e.g., Verma and Burkhardt, 2022).

Aircraft and spaceborne measurements have provided detailed properties of contrail cirrus. Firstly, contrail cirrus can be detected and separated from natural cirrus to some extent in in situ measurements by combining ice crystal microphysical data with observations of aircraft emissions such as nitrogen oxides (NO_x) or aerosols (Voigt et al., 2017; Voigt et al., 2021; Bräuer et al., 2021a). Schumann et al. (2017) and Heymsfield et al. (2010a) provide comprehensive overviews of contrail and contrail cirrus properties and extensive data sets exist on their microphysical properties (e.g. Petzold et al., 1997; Baumgardner and Gandrud, 1998; Jensen et al., 1998a, b; Voigt et al., 2010; Bräuer et al., 2021b), their particle shapes (Gayet et al., 2012; Järvinen et al., 2016; Sanz-Morère et al., 2020) and optical properties (Chauvigné et al., 2018), as well as the aviation influence on them (Jeßberger et al., 2013; Schumann and Graf, 2013; Marjani et al., 2022). Recent attempts used the reduced air traffic situation due to the COVID-19 pandemic to evaluate the aircraft impact on cirrus and climate (Gettleman et al., 2021; Li and Groß, 2021; Quaas et al., 2021; Schumann et al., 2021b; Meijer et al., 2022; Voigt et al., 2022). While the aircraft impact on clouds is confirmed by those studies, the magnitude of the reduced contrail cirrus forcing is variable and depends on the region, season and the method used to derive the impact. Some studies have taken the North Atlantic and North America with the

largest air traffic density as target regions, and analysed the temporal evolution~~diurnal cycle~~ of contrail cirrus coverage, outgoing radiation, and properties ~~during several contrail outbreaks~~ (Duda et al., 2004; Atlas et al., 2006; Haywood et al., 2009; Graf and Schumann, 2012; Duda et al., 2013; Minnis et al., 2013; Schumann and Graf, 2013).

Early climate models estimated contrail cirrus RF through associating air traffic with regional cirrus coverage and assumed equal radiative efficiencies of contrails and contrail cirrus (Stordal et al., 2005; Rädel and Shine, 2008). Later, the global climate models represented contrail cirrus as a separate cloud class (Burkhardt and Kärcher, 2011; Bock and Burkhardt, 2016). In Chen et al. 2012~~another study~~, contrail cirrus is simply treated as a source for the ice crystal budget of the natural cirrus, mixing the microphysical properties of contrail cirrus and natural ice clouds ~~(Chen et al., 2012)~~. Hence, despite substantial progress in recent years, the characterization of geometrical, optical, and microphysical properties of contrails and their evolution within natural cirrus fields as well as the calculation of the radiative impact are still subject to large uncertainties due to instrumental and model limitations and the large number of variables influencing the contrail life cycle (~~Voigt et al., 2017;~~ Chauvigné et al., 2018; Kaufmann et al., 2018; Rodríguez De León et al., 2018; Gierens et al., 2020).

In this study, we use in situ data measured during the Mid Latitude Cirrus (ML-CIRRUS) experiment (Voigt et al., 2017) from the German High Altitude and LOng Range Research Aircraft (HALO) and simultaneous remote sensing observations (Bugliaro et al., 2011; Vázquez-Navarro et al. 2013; Strandgren et al., 2017a) with high temporal resolution from the SEVIRI imager aboard the geostationary Meteosat Second Generation (MSG) satellite. In particular, we concentrate on one flight on 26 March 2014 over the North Atlantic Region (NAR) just off the coast of Ireland where most of the air traffic from Europe to the US and viceversa takes place. This situation enables us to investigate properties and radiative effects of ~~contrails,~~ contrail cirrus and ambient natural cirrus in an ideal contrail cirrus outbreak. In particular, we develop a new method to classify ~~ice crystals~~cirrus along the HALO flight track from in situ measurements based on enhanced NO aircraft gas emissions and ice number concentrations N into three representative classes: ~~that are representative for~~ (1) contrails, (2) contrail cirrus and (3) natural cirrus where the effect of aircraft emissions is not directly observable. For these classes we evaluate microphysical ice crystal properties ~~(effective radius, R_{eff})~~ and relate them to relative humidity over ice (RHi). ~~From satellite remote sensing we evaluate ice optical thickness (IOT), R_{eff} of the ice crystals, reflected solar radiation (RSR) and outgoing longwave radiation (OLR) along the flight path. Furthermore, we also develop~~ Satellite observations from MSG/SEVIRI are inspected visually to characterise the general cloud situation and confirm the presence of various contrails, in line with in situ measurements. In a new approach developed and for the first time presented in this paper, we determine the ~~determination of~~ ice cloud RF that combines in situ and satellite observations with a radiative transfer model (RTM). To this end, we use reanalysis data from ERA5 (Hersbach et al. 2020). Since ERA5 does not simulate the effect of air traffic on clouds, we collect atmospheric profiles of water vapour, liquid and ice clouds from this reanalysis and combine them with the in situ and spaceborne observations to provide inputs to the RTM to compute reflected solar radiation (RSR) and outgoing longwave radiation (OLR). After checking the consistency of our radiative transfer calculations with the corresponding RSR and OLR measured with the Geostationary Earth Radiation Budget (GERB) instrumentation, we are in the position to compute instantaneous RF of this special combination of clouds in the SW and LW spectral range ~~along the flight path of HALO~~ by ~~-~~ excluding the ice cloud layer ~~(contrails, contrail cirrus and natural cirrus) at the flight level~~ from the radiative transfer calculations, thus yielding a consistent ice-cloud-free irradiance. ~~In a second step~~To be specific, we ~~extend~~ operate these calculations to an area encompassing the HALO flight path to compute the diurnal cycle of RF in that region, thus exploiting the information from high resolution airborne measurements and broad and diurnal satellite observations for a holistic view on the radiation budget from this ideal case in the NAR.

Detailed information about airborne and satellite datasets, as well as cirrus remote sensing techniques and the RTM are presented in section 2. Microphysical properties of contrail cirrus and natural cirrus, consisting of cirrus classification, collocation of in situ and observed cirrus, and ~~further~~ differences between contrail cirrus and natural cirrus, are summarized in section 3. Radiative effects of contrail cirrus and natural cirrus, including the top-of-atmosphere (TOA) radiation estimation

method~~, detailed RTM calculations of RF along HALO flight~~, and the investigation of cirrus and RF spatial pattern are organized in section 4. Finally, in the summary and conclusions in section 5 we provide guidance about how to transfer our data evaluation techniques to future studies on radiative transfer calculations of contrails and contrail cirrus~~are provided in section 5~~.

2 Data and approaches

2.1 Airborne measurements

During ML-CIRRUS, the German research aircraft HALO was equipped with a comprehensive suite of novel particle measurement sondes, and obtained a broad dataset of microphysical properties of contrail cirrus and natural cirrus for process studies and climatological analyses. Ice number concentrations N, R_{eff}, size distributions, ice or liquid water content (IWC and LWC) and extinction are derived from measurements of CAS-DPOL (Cloud and Aerosol Spectrometer with Detector for Polarization) for particles from 3 to 50 µm and CIP (Cloud Imaging Probe) for the size range of 15 and 960 µm (diameter as the maximum dimension). CAS-DPOL measures the forward scattered light of particles when they pass through a laser beam (Baumgardner et al., 2011). The uncertainty of the particle size measurements is ±16% (Kleine et al., 2018). Using 64-element linear photodiode arrays, the CIP acquires two-dimensional shadow images of particles (De Reus et al., 2009). The size resolution is 15 µm with the uncertainty decreasing considerably with diameter, reaching ±15 µm when particles are larger than 50 µm. N from CAS-DPOL, denoted by N_{CAS} in the following, and from CIP (N_{CIP}) are also combined to an overall N between 10^{-4} and 10^{2} cm^{-3}~~that considers the particle size overlap of the two instruments~~. ~~The aspherical fraction of particles with R_{eff} larger than 3 µm measured by CAS-DPOL is determined by the ratio between perpendicularly polarized light and the forward scattering light. Based on measurements in the Aerosol Interaction and Dynamics in the Atmosphere (AIDA) cloud chamber described in Järvinen et al. (2016), particles with a polarization ratio larger than the 1σ range of size dependent thresholds are categorized as aspherical.~~ Validation of the measurements, ~~particular for the smaller spherical particles,~~ have been performed taking atmospheric and cloud chamber measurements into account (Braga et al., 2017a, b).

As for ambient conditions, the AIMS (Atmospheric Ionization Mass Spectrometer, Jurkat et al., 2016, Kaufmann et al., 2016) was applied to measure the actual water vapor concentration from ambient air using a backward heated inlet. The range of detection is between 1 and 500 ppm with an overall accuracy from 7% to 10%. Static pressure and temperature, measured by the BAHAMAS (Basis HALO Measurement and Sensor System, Krautstrunk and Giez, 2012) with an accuracy of 0.3 hPa and 0.5 K, were used to convert water vapor concentration to RHi with an uncertainty of 10 % to 20 % (Kaufmann et al., 2018).

During the mission, nitrogen oxide (NO) and the sum of all reactive nitrogen species (NOy) were measured using the AENEAS instrument (AtmosphEric Nitrogen oxides mEAsuring System). This dual channel instrument is based on the well-established chemiluminescence technique combined with catalytic conversion of the NOy components. It has been regularly operated on HALO during several missions (e.g., Ziereis et al. 2022). A detector identical in construction has also been operated on a commercial aircraft as part of IAGOS-CARIBIC (Stratmann et al., 2016). The statistical detection limit is about 7 pmol/mol for NO. The overall uncertainty depends on the ambient concentration of NO and ranges from about 8 to 6% for volume mixing ratios between about 1 and 0.5 nmol/mol. The time constant of the instrument for measurements in the upper troposphere is of the order of 1 s. ~~NO was measured by the conventional chemiluminescence technique using AENEAS (AtmosphEric Nitrogen oxides mEAsuring System chemiluminescence detector, Ziereis et al., 2000) as the aircraft tracer. The upper limit of the measuring range limit is 60 ppbv. The overall uncertainty is 8% for NO for concentration levels of 0.5 ppbv (Stratmann et al., 2006).~~ The time offsets of NO have been shifted based on ice number.

Backscatter profiles of clouds and aerosol were acquired by the lidar system WALES (Water vapor Lidar Experiment in Space, Wirth et al., 2009) at the wavelengths of 532 and 1064 nm. In this study backscatter is used to extract information about the cirrus cloud structures, such as cloud top height (CTH), geometrical depth and others. ~~Apart from the backscatter coefficient,~~

WALES also provides 2D measurements of the water vapor mixing ratio and aerosol particle linear depolarization ratio. The backscatter ratio and aerosol depolarization (perpendicular to parallel) (Biele et al., 2000; Esselborn et al., 2008) are used to create a cloud mask, which helps to discriminate for~~keep only~~ ice clouds. For these clouds the RHi is calculated from the measured water vapor mixing ratio and collocated model temperatures from the European Centre for Medium-Range Weather Forecasts (ECMWF). This instrument and method have also been applied by Groß et al. (2014) and Urbanek et al. (2018), who found that the lidar measurements were accurate when compared with in situ data. The statistical error in the retrieval of water vapor by WALES is estimated to be about 5% (Kiemle et al., 2008) and the ECMWF temperatures induce an error of around 10-15% in the final RHi values (Groß et al., 2014).

2.2 Satellite remote sensing

The Spinning Enhanced Visible and InfraRed Imager (SEVIRI) is the primary instrument aboard the geostationary MSG satellites, which provides observations of the Earth disk every 15 min from 3 solar and 8 thermal channels with 3 km sampling distance at nadir, and one High Resolution Visible channel with 1 km spatial resolution (Schmetz et al., 2002). We use MSG-3 / Meteosat-10 observations for the study on 26 March 2014 with a temporal resolution of 15 min.

2.2.1 CiPS

CiPS (Cirrus Properties from SEVIRI) detects cirrus with their transparency information and retrieves the corresponding CTH, ice optical thickness (IOT), ~~ice R_{eff}~~ and ice water path (Strandgren et al., 2017a). It consists of four artificial neural networks trained using SEVIRI thermal observations, CALIPSO (Cloud-Aerosol Lidar and Infrared Pathfinder Satellite Observations) cloud products, and ECMWF ERA5 surface temperature and auxiliary data. CiPS has been especially developed for thin cirrus and validated against CALIPSO. CiPS detects 20%, 70% and 85% of the ice clouds with an IOT of 0.01, 0.1 and 0.2 respectively. For IOT between 0.35 and 1.8 CiPS has a mean absolute deviation smaller than 50%. This value increases for IOT between 0.07 and 0.35. For CTHs larger than approx. 8 km, CTH has an absolute percentage error of 10%, with underestimation for CTH > 10 km at 50° N and overestimation for CTH < 10 km at the same latitude. An example is shown in Fig. 1.

2.2.2 GERB and RRUMS

The GERB (Geostationary Earth Radiation Budget) instrument measures broadband solar and thermal components which are subsequently converted to outgoing and reflected fluxes considering the cloud properties and surface type detected by SEVIRI (Harries et al., 2005). GERB's sampling distance is larger than that of SEVIRI with a spatial resolution of 44.6 km × 39.3 km but the same image repeat ~~s the~~ cycle of 15 min. During the processing, the finer spatial resolution of the SEVIRI data is used to improve the original GERB resolution and results in GERB products for 3x3 SEVIRI pixels. In general, the GERB SW and LW fluxes are found to be 7.5% higher and 1.3% lower respectively, compared to products from the Clouds and the Earth's Radiant Energy System (CERES), whose data records are from polar orbiting satellites (Wielicki et al., 1996). The bias of CERES is estimated to 1% and 0.5% for OLR and RSR, respectively.

Based on a linear regression and a neural network, an algorithm named RRUMS (Rapid Retrieval of Upwelling Irradiances from MSG/SEVIRI) was also developed, which estimates OLR and RSR at TOA from SEVIRI at pixel levels. RRUMS shows excellent agreement with OLR from CERES within 1% and a systematic overestimation of RSR from CERES or GERB of 5% to 10% in the worst cases under high viewing angles (Vázquez-Navarro et al., 2013).

~~2.2.3 Collocation~~

~~We exploited ground positions of ice clouds from ML-CIRRUS measurements and CTHs estimated from WALES observations to collocate the clouds probed by HALO with the SEVIRI observations. Thanks to the 15-min repeat cycle of the~~

~~geostationary imager, temporal shifts up to 7.5 min result from this procedure. Since the temporal frequency of in situ observations is 1 Hz, various HALO values are located inside each SEVIRI pixel. Of course, HALO measurements do not fill SEVIRI pixels such that they are representative only of a part of them. In general, statistics or time series of observations are produced with the original temporal resolution of the given instrument. However, when one in situ IOT or R_{eff} value for a SEVIRI pixel is needed (see e.g. Sect. 3.2) then averages are computed.~~

2.3 Radiative transfer model

To calculate broadband solar and thermal irradiances at TOA for ice particles~~ probed during the HALO flight~~, ~~a~~ the sophisticated radiative transfer package libRadtran is used (Mayer and Kylling, 2005; Emde et al., 2016). Water and ice clouds are represented in this model ~~detailly~~ in detail and realistically. Optical properties of water droplets are computed using the Mie theory and tabulated as a function of wavelength and R_{eff}. Ice crystals are not spherical in shape and habits (Letu et al., 2016), and for this simulation the parameterisation of Baum et al. (2011) for ice crystal habits has been employed to define the conversion from optical to microphysical properties. In analogy to the MODIS products (Yang et al., 2018), we select rough aggregates for ice crystal shape (see Sect. 4.2 for a discussion about this choice). The selected one-dimensional radiative transfer solver is DISORT (Discrete Ordinate Radiative Transfer) 2.0 by Stamnes et al. (2000) with 16 streams. ~~And~~ LibRadtran recommends the REPTRAN band parameterization with a spectral resolution of 15 cm^{-1} for spectral calculations (Buehler et al., 2010; Gasteiger et al., 2014).

We exploited positions of ice clouds from ML-CIRRUS measurements and CTHs estimated from WALES observations to collocate the clouds probed by HALO with the SEVIRI observed contrail cirrus and natural cirrus. We notice that satellite observations are functions of both time and space. Since the temporal frequency of in situ observations is 1 Hz, various HALO measurements are located inside each SEVIRI pixel. In general, time series of observations are produced with the original temporal resolution of the given instrument.

3 Microphysical properties of contrail cirrus and natural cirrus

In this section we describe how airborne data from HALO and images from satellite remote sensing ~~outputs from CiPS~~ are combined to understand microphysical properties of contrail cirrus and natural cirrus, and the corresponding variation when contrails transit into contrail cirrus within the contrail life cycle.

3.1 General situation

In the night and the very early hours of 26 March 2014 a ridge cirrus cloud band built up North of Ireland down to the Southern tip of Portugal (Fig. 1). ~~North of Ireland~~ Close to Iceland as well as to the South-West of Ireland this cirrus cloud ~~is thicker~~thickened (optical thickness larger than 1 at 10:45 UTC, Fig. 1d). ~~while~~ While exactly off the coast of Ireland, in coincidence with the eastbound morning and westbound afternoon air traffic to and from the US, many linear structures can be seen in SEVIRI observations (Fig. 1, especially Fig. 1b where brightness temperature differences (BTD) between the SEVIRI channels at 10.8 and 12.0 µm are shown~~ is enlarged in Fig.2~~) and the ice cloud is thinner (optical thickness around 0.3 at 10:45 UTC). Please notice that Fig. 1 is enlarged in Fig. 2. Considering that the peak of eastbound morning air traffic is approx. at 3 UTC (Graf and Schumann, 2012), under favourable conditions with low temperature and high humidity~~these~~ contrails induced from these aircraft are expected to form and live for hours such that they can be ~~might be those~~ identified in MSG observations in the morning of the same day~~in this study, withsome older contrails from the westbound traffic in the afternoon of 25 March, which however peaks already at 13 UTC~~. This cloud band evolves with time towards the South, and in correspondence of the Ireland coast the ice clouds dissipate around noon~~until approx. 14 UTC~~. In addition, this thin bluish/violet ice cloud band partly overlaps with a liquid water cloud field below (yellowish clouds in the false colour

composite in Fig. 1a). ~~At the same time, the weather condition over Europe is characterized by a cyclone affecting the Mediterranean Sea with most of mainland Europe covered by liquid clouds and cirrus over the Eastern Atlantic Ocean.~~

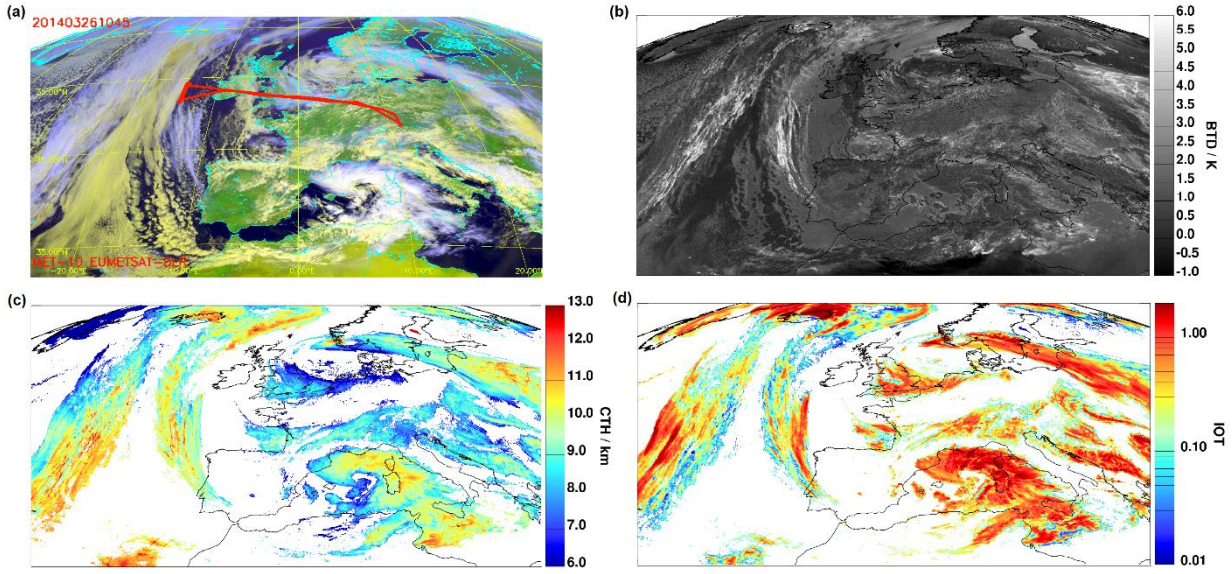

Figure 1: (a) The false color RGB image from MSG/SEVIRI overlapped with the HALO flight track on 26 March 2014 at 10:45 UTC showing Europe and the Eastern part of the North Atlantic Ocean, (b) corresponding 10.8 µm and 12.0 µm brightness BTD (K) with overlaid ice clouds, (c) CTH and (d) IOT from CiPS

Due to its approx. 3.5 km × 4.5 km spatial resolution~~(Sect. 2.2)~~, SEVIRI can only observe contrails that have already grown larger (and thicker) while young contrails are usually missed (Mannstein et al. 2010). ~~Thus, the presence of these numerous persistent contrails as well as the simultaneous evolution of the cloud band indicate that contrails and contrail cirrus / persistent contrails maybe embedded in or on top of / below cirrus particles of natural origin. The relative vertical location of contrails and natural clouds is difficult to determine from the passive remote sensing perspective as well as the origin of ice particles, unless the typical linear shape of contrails can be directly observed.~~ Nevertheless, the satellite observations indicate that because of these favourable meteorological conditions and the relatively high air traffic density in this region, contrails from various aircraft~~s~~ could form over a long time period (~12 h) that ~~might~~ overlap ~~in the vertical direction or that are formed inside / on top of / below~~with “the remnants” of previous contrails. Thus, air traffic in this area has~~could have~~ a strong impact on cloudiness on the day under study.

On 26 March 2014 the HALO aircraft started from Oberpfaffenhofen in Germany ~~for the first flight of the ML-CIRRUS campaign (Voigt et al., 2017)~~ at approximately 05:30 UTC and probed the cirrus over NAR from around 08:00 to 11:30 UTC with a race track pattern between approx. 51.5°N and 54°N at a longitude of ca. -14°E (-13.6 to -14.4°E), see the flight track in Fig. 1a and also Voigt at al. (2017, Fig.4). In this area, HALO flew ~~3 in situ legs split by~~ 3 lidar legs almost perpendicular to the NAR tracks (07:57 UTC - 08:35 UTC, south to north, 09:17 UTC - 09:30 UTC, north to south, and 10:21 UTC - 10:52 UTC, south to north), each followed by in situ legs at different altitudes.

Figure 2 presents the temporal variation of contrails and surrounding clouds with ~~the~~ one ~~real-time~~ HALO in situ/lidar leg at close time and air traffic data 2 to 3 hours before from 08:30 ~~08:00~~ (~~HALO entering the NAR~~the first in situ leg) to ~~12:00~~ 10:30 UTC (~~HALO leaving the NAR~~the third lidar leg). ~~For the sake of presentation, we show hourly plots, but for the analyses exposed in the paper we use the full 15 min resolution. To each SEVIRI observation we assign the closest HALO measurements (Sect. 2.2.3) that thus differ in acquisition time from the SEVIRI images by at most 7.5 min. The HALO path already flown - i.e. older that the acquisition time of SEVIRI minus 7.5 min - is plotted in red, while the HALO flight track corresponding to the current satellite images - i.e. HALO path in the time range between SEVIRI acquisition time plus/minus 7.5 min - is plotted as blue. Notice also the nominal slot time of SEVIRI of e.g. 09:00 UTC corresponds to a real acquisition time of approx. 09:12 UTC.~~ In addition, the area around the flight path is investigated in Sect. 4.~~4~~2 in more detail but that serves here as orientation

to easily capture the temporal evolution of the ice clouds. The aircraft flight to and from the Europe. In the ~~brightness temperature difference (~~BTD~~)~~ images – where SEVIRI brightness temperatures at 10.8 µm and 12.0 µm are subtracted from each other - the black areas are caused by the low-level clouds, while the bright pixels correspond to thin cirrus. Small ice crystals, for instance in contrails, correspond to the largest BTDs. The wind speed in the east-west direction fluctuates around 0 while winds in the north-south orientation drive the ridge cloud to move southwards (blue arrows in Fig. 2 indicate wind direction at 225 hPa from ERA5). From 08:30 UTC, many thin lines (contrails) are seen in the false colour RGBs in the first column in Fig. 2, where also the HRV channel was used. They run parallel to most air traffic routes (blue diamonds in the second column, S1) and are intersected perpendicularly by the HALO route. Some of the contrails are also visible in the BTD pictures (the second column in Fig. 2), that have a lower spatial resolution than the HRV channel, thus indicating the presence of small ice crystals ~~that are intersected perpendicularly by the HALO route (top row)~~. T~~However, t~~hese contrails form a thin cirrus layer, ~~with~~ potentially of anthropogenic origin but also with natural~~ly~~ ~~nucleated~~ ice ~~crystals~~ clouds (see discussion of Fig.3 below). In the South, the ridge cirrus is thicker and no contrails can be observed. At 09:30 UTC, the flight area is dominated by contrails. With time, from 08:30 to 10:30 UTC the typical contrail lines become always fainter and less in number. Thus, contrails begin either to dissipate ~~(see low IOT)~~ or to lose completely their linear shape due to wind shear such that they turn out to be undistinguishable. However, contrails can be still observed in the north-eastern part of the satellite images at later times.

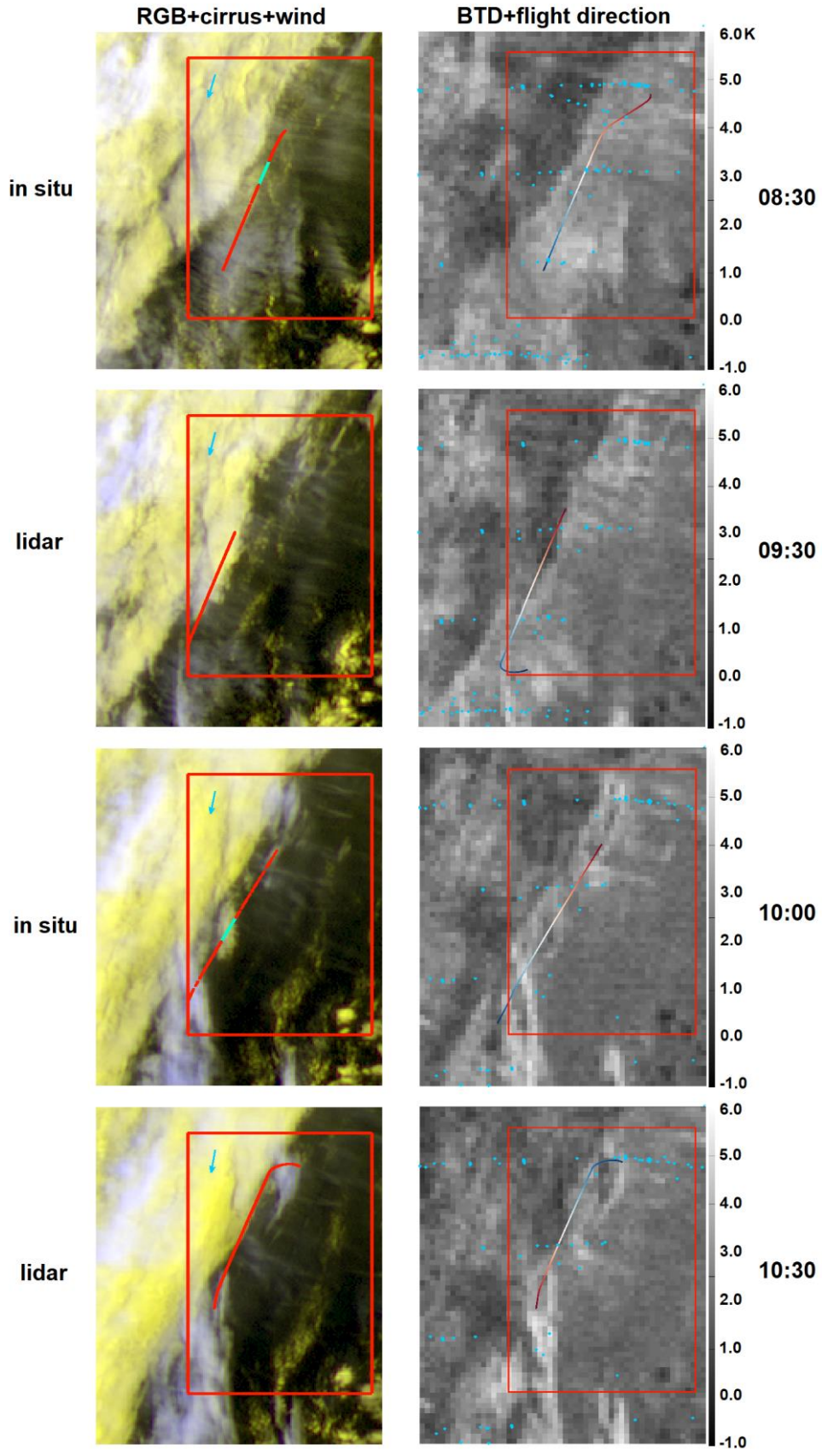

Figure 2: ~~Temporal variation~~Time series of contrail cirrus and surrounding clouds from MSG/SEVIRI observations over the NAR corridor on 26 March 2014. The first column: RGB-composite with overlaid cirrus, low-level liquid clouds pixels and in situ/lidar HALO leg at close time. The red and green line of the HALO flight track represent contrail cirrus and natural cirrus, respectively. The blue arrow indicates the wind direction almost perpendicular to the line shaped structures of the contrail cirrus. The second column: 10.8 µm and 12.0 µm BTD (K) with overlaid cirrus pixels. Blue points show air traffic dataset interpolated to MSG grid from M3 and NATS. The color of the HALO flight track indicates the flight direction. HALO flies from red to blue part. ~~: IOT from CiPS.~~ Top to bottom: 08:30, 09:30, 10:00 and 10:30 UTC. The red area is investigated in Sect. 4.2.

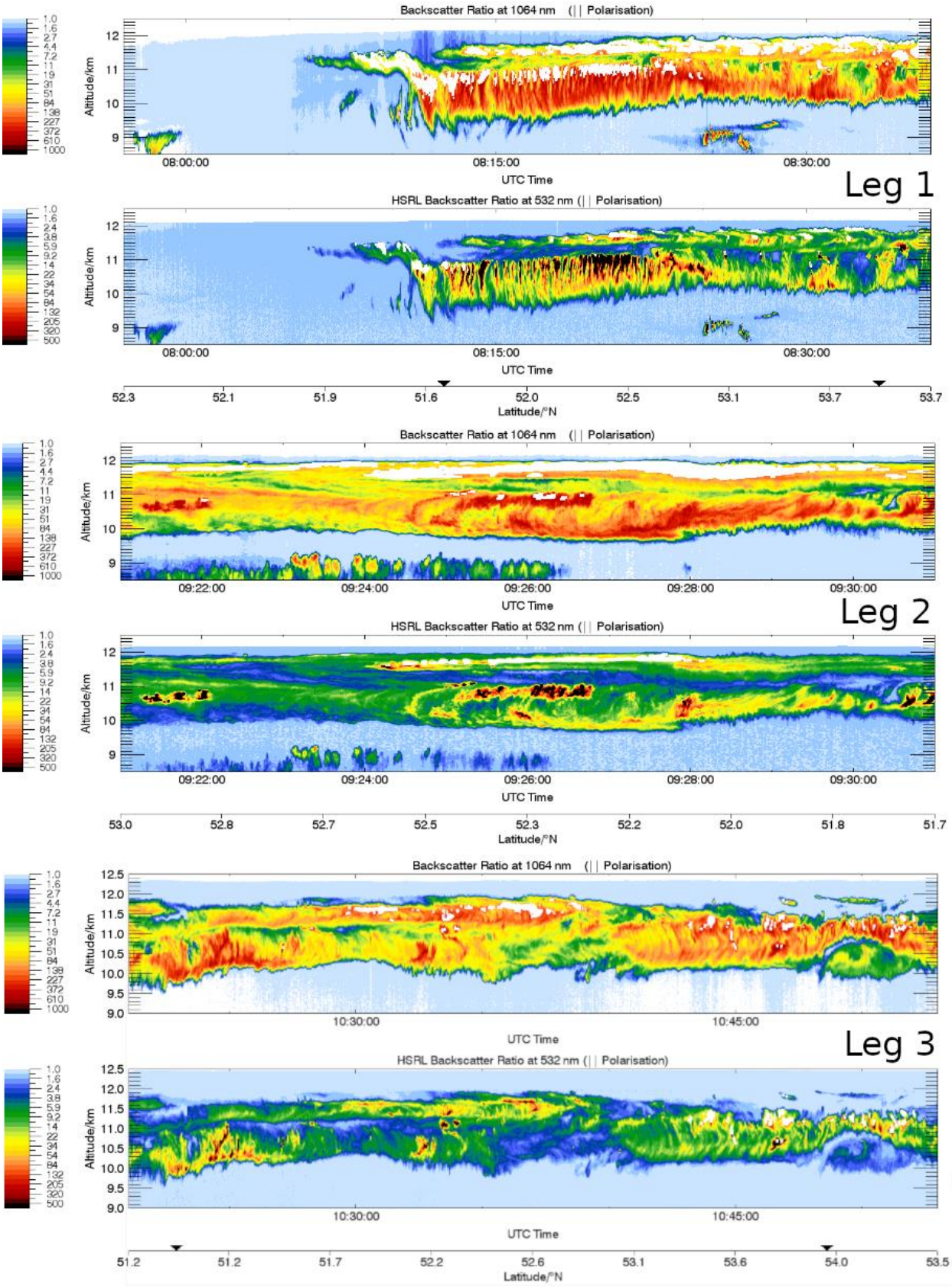

Figure 3: The three panels show the three lidar legs with backscatter ratios at 1064 nm and 532 nm. ~~**Leg 2 is much shorter than the other two legs, and leg 1 starts before 8:30 UTC, which is the start time of the evaluation presented in the paper.**~~

Figure 3 presents the backscatter ratio at 532 and 1064 nm from the WALES lidar measurements in that sequences. The lidar data show that the geometrical thickness of high-level clouds reduce~~d~~ from ~2.0 km at 08:30 UTC to ~1.5 km at around 11:00 UTC. The temporal evolution of CTH from WALES shows that the cloud firstly reached up to approximately 12 km and

slowly descended to slightly above 11.5 km, with backscatter values becoming smaller with time, in line with the passive observations that indicate dissipation of the cloud during the day. ~~Mid-level clouds appeared occasionally at a height between 4 and 6 km (not shown). In the following~~ For the investigation of contrails from in situ measurements we concentrate on the time period between 08:30 and 11:30 UTC, but we extend this time to cover the period from 6:00 UTC to 14:00 UTC in Sect. 4.2.

Considering the three WALES legs in more detail (Fig. 3), ~~one can observe~~ in leg 1 between ~~ca.~~ 08:10 and 08:25 UTC there is a series of connected fall streaks with high backscatter at a height of ~~approx.~~ 11 km below a thin ice cloud layer top at 12 km. These structures resemble those in the large eddy simulations by Unterstrasser et al. (2017a, b) where they considered contrails ~~formation followed by homogenous nucleation of a~~within natural cirrus ~~cloud~~. ~~This might be the case here as well: contrails formed first and reduced RHi and then the cirrus formed around it. However, contrails are so many and so close to each other that undisturbed ice clouds do not seem to be visible.~~ Thus, these bright spots with their fall streaks can be very probably identified as contrails, with many small ice particles causing high backscatter and with larger ice crystals sedimenting down. For leg 1, these contrails ~~seem to~~ make up the majority of the cloud in this temporal interval~~, with maybe homogeneous nucleation on top, although some isolated spots are observable in the top ice layer as well~~. The presence of developed fall streaks is a hint that these contrails are ~~not very young~~aged (> 30 min). Unfortunately, the high WALES backscatter inhibits the determination of RHi (Fig. S1) for these bright spots, but the upper level of the clouds, just below the potential contrails, show ~~frequent~~ occasional ice supersaturation, with RHi above 100%. ~~In the lower cloud part, where many ice crystals are still encountered, RHi is below saturation, in large parts also below 90%.~~

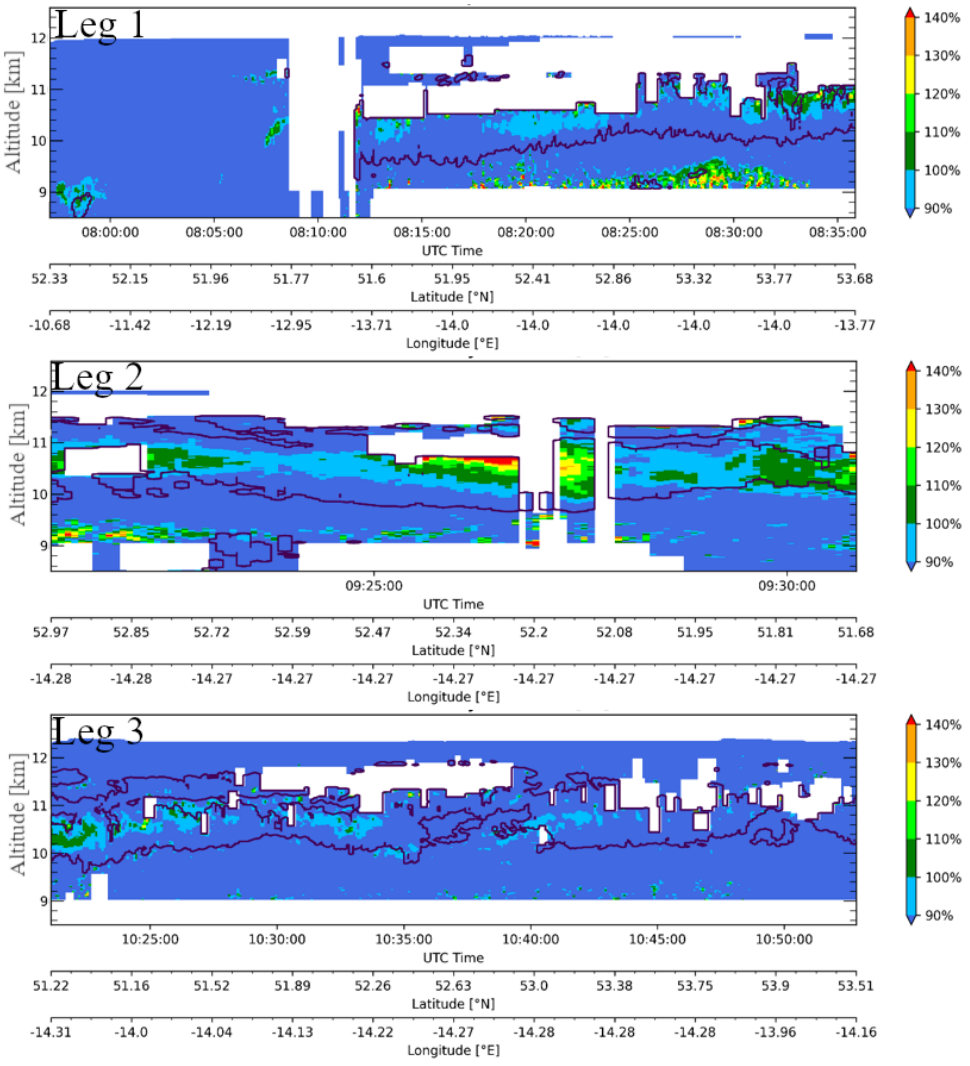

~~**Figure 4: The three panels show the RHi from Fig. 3 in more detail. The black contour represents the cloud edge. White areas are due to lack of measurements in these regions, because of detector saturation.**~~

Lidar leg 2, much shorter than the other two, also shows the presence of some spots with elevated backscatter ratios, although less numerous, at an altitude of ~~ca.~~ 11 km at ~~around~~ 09:26 UTC. Unlike leg 1, many high backscatter spots do not show extended fall streaks, suggesting the presence of younger contrails in addition to older ones. ~~This is supported by the fact that corresponding RHi in Fig. 4 reaches very high levels (RHi > 140%). , which makes natural nucleation events possible.~~ Furthermore, the top ice layer above ~~ca.~~ 11.5 km also contains some very high backscatter areas. Finally, also above 9 km some clouds are visible that resemble contrails (or a dissipating cirrus). Thus, in this leg the contrail-like structures do not fill the entire cloud as in leg 1, but there are indications of young and older contrails, ~~maybe~~ in addition to natural cirrus. The last lidar ~~leg~~ leg 3 ~~–~~took place ~~approx.~~ 1 h later and also shows various bright spots at different levels, from 10 to almost 12 km, and elongated vertical structures that remind of those in leg 1. The cloud as a whole is slightly lower than that in leg 1 with ragged edges especially at its lower border, suggesting that the cloud is sublimating and thinning out. This is confirmed by the RHi observations of WALES for leg 3 in Fig. S2, where subsaturation is indicated especially at the lower and upper edges, while around 10.5 km at selected locations RHi reaches saturation~~, at least there where RHi could be determined (in Fig. 2 CiPS also shows a decreasing cirrus cloud cover with time). In the upper part of the cloud, where RHi could not be determined, some bright spots are also observed. Overall, during all three lidar legs RHi is below saturation in large parts of the cloud. Finally, it is interesting to note that many of the bright spots appear at latitudes around 52°N corresponding to the southern part of the race track flown by HALO. Of course, one has to consider that these 3 lidar legs were not flown at the same position and that the cloud evolved in time due to microphysical processes and dynamics~~. T~~herefore, t~~hese WALES measurements are indicative~~representative~~ for the cloud probed between 08:00 and 11:30 UTC but ~~can neither be directly intercompared nor~~ cannot directly be compared to in situ observations taken at different times in between.

3.2 Properties of contrails, contrail cirrus and natural cirrus

~~In this region of sustained air traffic, with aircraft flying westbound to the US in the afternoon and eastbound to Europe in the morning, new contrails might form in the ice cloud remnants of previous contrail cirrus generated by earlier aircrafts. We use in situ measurements to distinguish between contrails, contrail cirrus and natural cirrus at the flight level of HALO. Notice however that we cannot unambiguously attribute cirrus to "natural cirrus" since both old contrail cirrus and nucleation on natural or anthropogenic aerosols transported from other sources might have taken place. At first, we consider in Fig. 5a all in situ measurements to obtain a general overview of R_{eff} against N from the combination of CAS and CIP about the cloud properties collected during the three legs. In this combined dataset, one can notice first that both R_{eff} and especially N are not particularly high. While R_{eff} up to 60 µm are encountered in natural cirrus clouds and low R_{eff} <5 µm are typical for contrails, N in contrails can grow much larger than 10-20 cm^{-3} as seen here (see discussion in Sect. 3.2.1). Furthermore, it is evident that R_{eff} lower than approx. 30 µm cannot be effectively detected by CIP while the CAS instrument is not able to identify ice number concentrations N lower than 0.01 cm^{-3}. As a result, there is a range of small N and small R_{eff} that cannot be observed in this study (indicated in Fig. 5a as "No data"). Nevertheless, in general Fig. 5a shows that low concentrations are associated with R_{eff} up to 60 µm, and most values concentrate around 45 µm, with increasing concentrations R_{eff} becoming smaller and falling below 10 µm. Only few observations correspond to high N and low R_{eff} and they are expected to represent contrails. Thus, it is a quite homogeneous distribution of R_{eff}, with most occurrences between 20 and 45 µm, but also with a smaller peak for R_{eff} < 10 µm. N extends over various orders of magnitude, with most occurrences between 0.01 and 0.5 cm^{-3}. Single vertical stripes for N close to 0.02 cm^{-3} are due to the CAS resolution (sampling volume).~~

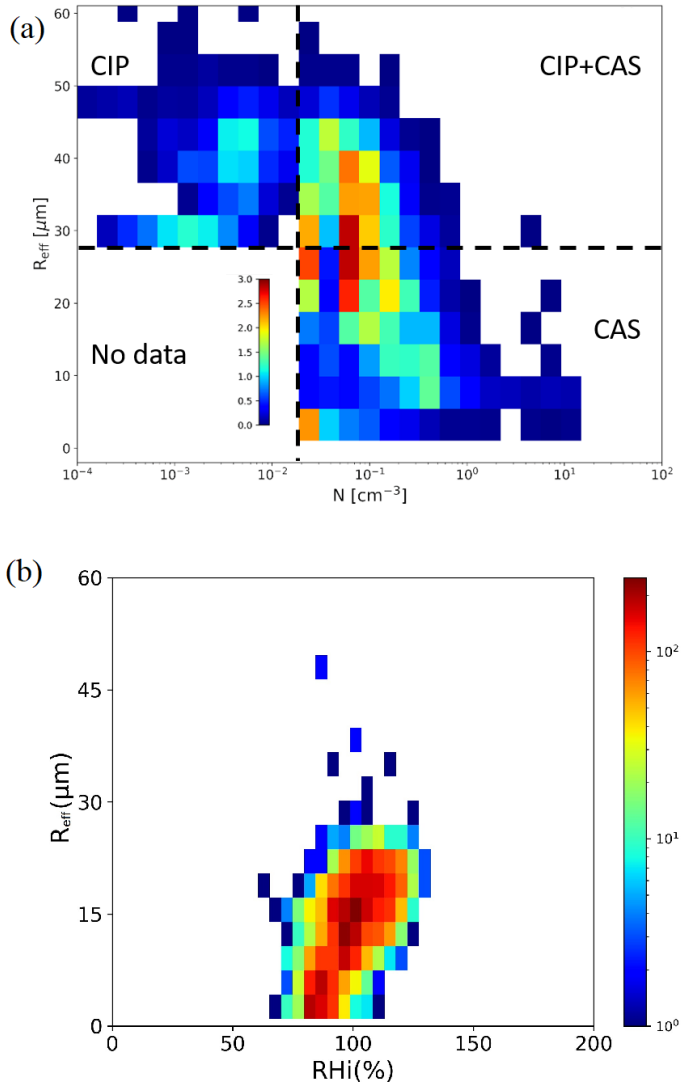

~~Figure 5: (a) Combined occurrences for R_{eff} and their corresponding N (particle concentrations from the cloud probes CAS and CIP) for all 1-sec data between 08:30 and 11:30 UTC. (b) R_{eff} occurrence distribution versus RHi.~~

~~Figure 5b also shows that over the entire flight path R_{eff} increases with RHi, as ice supersaturation supplies the water vapor for the growth of ice crystals, while subsaturated conditions lead to sublimation and evaporation. Nevertheless, still many ice crystals are observed in subsaturated conditions.~~

3.2.1 Identification of contrails and contrail cirrus and natural cirrus,

In this section, we improve a method already used in Voigt et al. (2010)~~This section provides a new method~~ to identify ~~in situ measurements~~ where aircraft emissions are fresh, older or not ~~a~~detectable by using in situ measurements. These three situations are assigned to ~~younger~~ contrails, ~~older contrails (~~contrail cirrus~~)~~ and unperturbed cirrus, also called natural cirrus. The goal ~~of this new method~~ is to investigate microphysical and optical properties of these ~~three ice cloud classes~~clouds. Figure 4 shows the full sequence of the airborne in situ measurements of N (N_{CAS}, N_{CIP}), R_{eff}, NO, cirrus (identified using the method in this Sect.), RHi, latitude and altitude as a function of time between 08:30 and 11:30 UTC. N for both instruments, CAS and CIP (N_{CAS} and N_{CIP}) and R_{eff} (Fig. 4a, b) indicate the occurrence of cirrus at the flight levels between 10 km and 13 km (Fig. 4g). ~~Many peaks of N up to or above 1 cm^{-3} have been measured. These values are not characteristic for young contrails, where N reaches up to > 1000 cm^{-3} in the first seconds/minutes after formation (Schröder et al., 2000; Kleine et al., 2018) or dilutes to 100 to 300 cm^{-3} after 5 to 10 min (Voigt et al., 2010; Voigt et al., 2017). The contrails probed here are more than 1 h 30 min old,~~ A~~a~~ccording to the dilution equation by~~of~~ Schumann et al. (2017) and assuming ~~under the simple assumption of~~ 1000 particles/cm^3 ~~when emissions past the aircraft engine~~ for 1s-old contrail, many contrails probed here are more than 1 h old.

~~Schröder et al. (2000, their Table 2) also show N ~10–20 cm^{-3} for contrail cirrus older than 30 min. Unterstrasser et al. (2017a) simulate mean N of 20 cm^{-3} after 5 min (labelled as t = 0 h in their paper) falling below 1 cm^{-3} after 2 h of lifetime. Finally, Bock and Burkhardt (2016) find N < 1 cm^{-3} in a contrail cluster after 5.5 h lifetime.~~ Furthermore, ~~the fact that~~ some contrails are also visible in the low-resolution MSG/SEVIRI satellite images (BTDs in Fig. 2) ~~is another indication that these persistent contrails are~~and therefore at least 1-2 h old (Vázquez-Navarro et al., 2015). ~~Figure 6c shows NO concentration which is produced during the combustion of kerosene. It can also be observed in the UT after fast transport from the boundary layer through convection or in lightning or wildfires. Measurements of NO have been performed continuously inside clouds and also during the lidar legs, where HALO was flying higher in the lower stratosphere (LS).~~ Figure 4c thus shows variable NO concentrations and various peaks ~~of different heights~~. Since other sources of NO are unlikely in this situation (no thunderstorms in the previous 12 h, no wildfires), we assume that the NO concentration increases correspond to aviation exhausts, with ~~of course~~ different peak height~~s differences being~~ caused by various factors such as contrail age, dilution and aircraft type (Voigt et al., 2010; Jurkat et al, 2011; Jeßberger et al., 2013; Schumann et al., 2013). In fact, after the emission, NO is mixed with the surrounding air and ~~the dilution of this gas increases~~dilutes with increasing plume age such that its measured mixing ratio can be used as a rough indication for contrail age~~, with high concentrations indicating younger plumes~~. ~~We exploit these considerations about NO combined with the fact that~~ As for contrails, initial ice particle concentrations N are high due to the high number of soot particles emitted by the engine (Schlager et al., 1997; Kleine et al., 2018; Bräuer et al., 2021a) ~~when a contrail is formed, but~~ and N decreases due to dilution (Schumann et al., 1998) and further processes (Bier et al., 2017; Unterstrasser et al., 2017a)~~ in the course of its temporal evolution~~. High NO emissions without coincident ice crystal observations correspond to situations where the Schmidt-Appleman criterion is not satisfied and no contrail is formed. This study, similarly to Voigt et al. (2010), uses N and NO ~~as criteria to classify ice crystal observations in the following way.~~to evaluate contrail evolution.

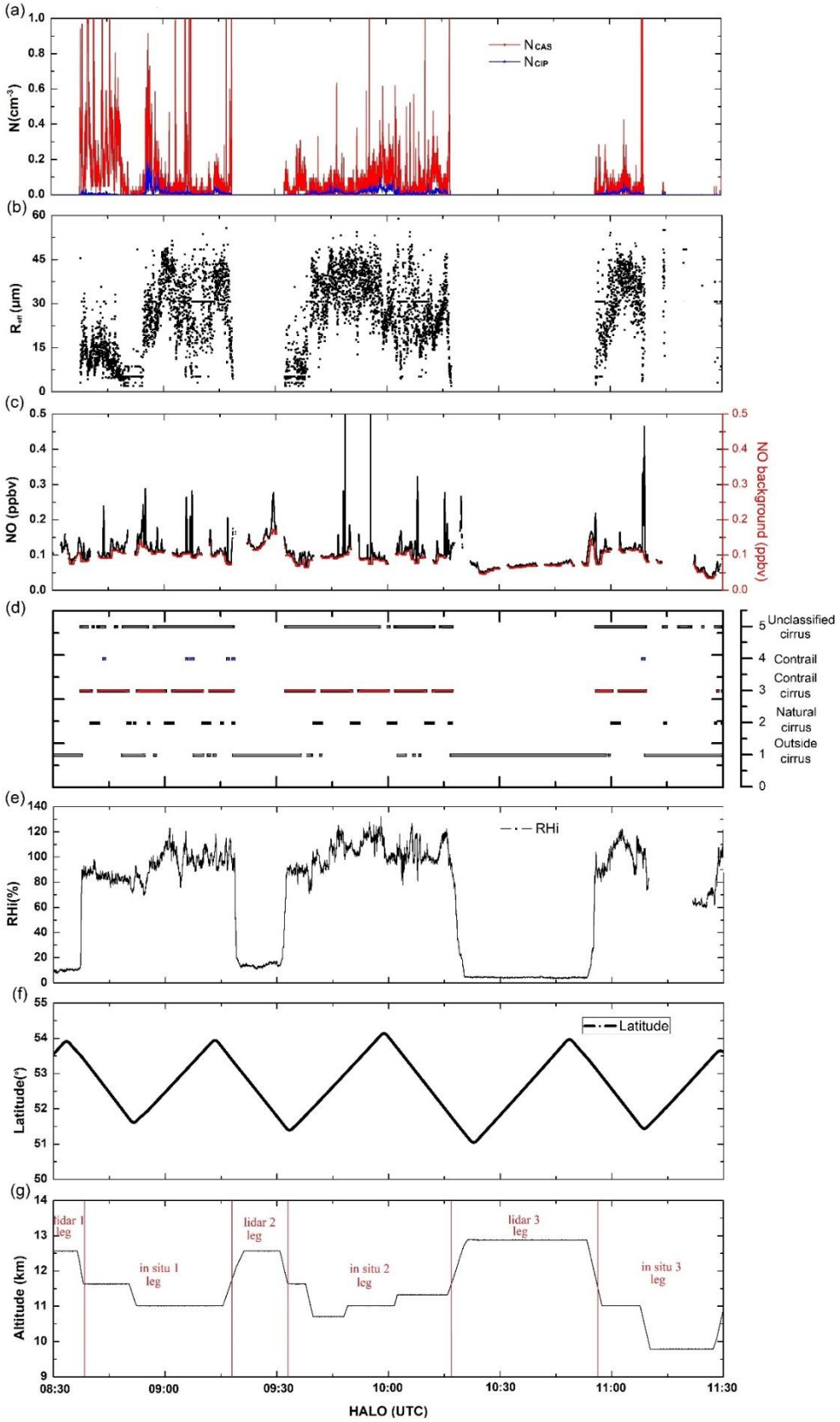

Figure 4: In situ measurements of HALO on 26 March 2014 over North Atlantic region, including (a) N ice number concentration > 3 μm~~for particles larger than 3 μm~~, (b) R_{eff}, (c) NO and NO background, (d) cirrus classification, (e) RHi, (f) flight latitude, (g) altitude.

First, we determine dynamically the NO background concentration $NO_{b~~ackground~~}(t)$ at a given time t by taking the minimum NO value in a 60-second sliding window around this time (Fig. 4c):

$$NO_{b~~ackground~~}(t) = min_{-30s \leq \Delta t \leq 30s} NO(t + \Delta t) \quad (1)$$

$NO_{background}(t)$ takes care of the natural variability of NO in this situation, since other NO sources that could produce NO peaks are excluded here (see beginning of this section). Notably, we use the RANSAC algorithm (Fischler and Bolles, 1981) to interpret NO outliers and confirm that they haven't hit the NO background but the peaks of NO values. The difference between $NO_{background}(t)$ and the NO(t) curve at each time t is termed $\Delta NO_{peak}(t)$

$$\Delta NO(t) = NO(t) - NO_{background}(t) \quad (2)$$

and describes the deviation of the NO curve from the background or the NO peak height above the background. NO is thus in this classification as the tracer for aircraft emissions. In a further step we consider ice number concentration N to classify contrails. However, when using N we have to consider that in the lower left portion of Fig. 5a no data is available. Thus, we consider only the right part of Fig. 5a where the full range of R_{eff} could be measured. In doing so we lose all cirrus clouds (usually natural cirrus) with higher R_{eff} (> 30 µm) and small N (< 0.03 cm^{-3}) in the upper part of Fig. 5a and also those cirrus clouds with low R_{eff} and low N (no data in Fig. 5a).

In accordance with Table 1, we first distinguish measurements in cirrus from "1. outside cirrus" when N_{CAS} and N_{CIP} are zero in step 1, and then separate "3. contrail cirrus" and "4. contrails" from "2. natural cirrus" when NO is higher than the background and N_{CAS} or N_{CIP} is larger than 0.03 cm^{-3} (see discussion of Fig. 5a and Fig. 6a) in step 2, reflecting the impact of air traffic. Contrail cirrus (older contrails) is separated from younger contrails by assuming a stronger NO footprint (lower dilution) in contrails. The rest is labelled as "5. unclassified cirrus" in step 3. This class contains on one side those clouds mentioned above that we cannot classify and likely consists mainly of natural cirrus. On the other side, ice cloud measurements with high ΔNO_{peak} (> 0.14 ppbv) but moderate N ($N_{CAS} \leq 0.4$ cm^{-3}) do also fall in this category and should represent observations in younger plumes where few ice crystals could form (maybe because temperature is close to the Schmidt-Appleman criterion) or because ambient air is subsaturated leading to the evaporation of a considerable fraction of newly formed (small) ice crystals. Summarised, natural cirrus is identified when ice crystals are present with either N_{CAS} or N_{CIP} larger than 0.03 cm^{-3} and NO close to the background value, i.e. $\Delta NO_{peak} \leq 0.02$ ppbv; contrail cirrus is characterised by moderate values of NO, i.e. 0.02 ppbv < $\Delta NO_{peak} \leq 0.14$ ppbv, and N_{CAS} or $N_{CIP} > 0.03$ cm^{-3}; contrails are assumed to consists of many small ice crystals, $N_{CAS} > 0.4$ cm^{-3}, and high NO peaks, i.e. $\Delta NO_{peak} > 0.14$ ppbv. The remaining cirrus is denoted as "unclassified cirrus".

Table 1: Cirrus classification according to microphysical properties (N), and tracer measurements (NO) measured by instruments aboard HALO.

	Designation	N / cm^{-3}	ΔNO_{peak} / ppbv	Note
1.	Outside cirrus	$N_{CAS} = 0$ and $N_{CIP} = 0$	Any value	Step 1
2.	Natural cirrus	$N_{CAS} > 0.03$ or $N_{CIP} > 0.03$	$\Delta NO_{peak} \leq 0.02$	Step 2
3.	Contrail cirrus	$N_{CAS} > 0.03$ or $N_{CIP} > 0.03$	$0.02 < \Delta NO_{peak} \leq 0.14$	
4.	Contrails	$N_{CAS} > 0.4$	$\Delta NO_{peak} > 0.14$	
5.	Unclassified cirrus	The rest		Step 3

The threshold values for NO_{peak} (0.02 ppbv and 0.14 ppbv) have been determined from the NO_{peak} distribution. NO_{peak} distribution decreases from 0.0 to 0.48 ppbv, with the largest bins being the first and the second one ($0 <= NO_{peak} < 0.02$ ppbv). Thus, we consider NO to be close to the background value when $NO_{peak} <= 0.02$ ppbv and to contain additional NO when $NO_{peak} > 0.02$ ppbv. The NO occurrences sink by two order of magnitude (from 10^3 to 10^1) until NO_{peak} equals 0.25–0.30 ppbv. After these values, a tail of relatively seldom high NO_{peak} values (occurrences~10^1) is observed. In order to distinguish old emissions from younger ones, we select the threshold of NO_{peak}=0.14 ppbv, in the middle of the range mentioned above. Thus,

~~NO_{peak} between 0.02 and 0.14 ppbv are assumed to capture only older emissions, leaving high NO peaks as well as moderate ones in the range NO_{peak}>0.14 ppbv (representing the highest 5% NO_{peak}). For the determination of N thresholds for contrails we proceed similarly. In particular, N_{CAS}<0.03 cm^{-3} contains an order of magnitude more observations than the next one. Then, N_{CAS} occurrences decrease by more than 2–3 orders of magnitude from 0.03 to 0.78–0.84 cm^{-3}. Again, we take a value in the middle (0.4 cm^{-3}) as separation between high N_{CAS} peaks attributable to contrails and moderate values of N_{CAS}<0.4 cm^{-3} that we assign to older contrails/contrail cirrus. Please notice that N and NO are selected independently. Notably, these values are just valid for this flight sequence over the NAR on 26 March 2014 during the ML-CIRRUS campaign.~~ The determination of ΔNO and N thresholds are explained in S3 and Fig. S2. In total, from 08:30 to 11:30 UTC for each aircraft measurement with a frequency of 1 Hz we have classified 49 contrail observations, 1018 contrail cirrus observations and 2342 natural cirrus observations in Fig. 4d from in situ measurements. Unclassified cirrus encompasses 2472 cases, with 94 of them having ΔNO_{peak} > 0.14 ppbv. ~~This means that a~~At least 31~~18~~% of all ~~measurements~~ classified cirrus ~~were~~was in contrails or ~~/~~contrail cirrus, confirming the indications gained from MSG and WALES in Sect. 3.1 about the large amount of contrails. ~~We finally remark that MSG/SEVIRI satellite observations are left unused for this classification . since the distinction between contrail cirrus and natural cirrus from satellite observations is inherently difficult due to the typical characteristics of young contrails - large N - cannot be measured by passive sensors.~~

~~As an example, we first illustrate a contrail encounter between 08:43 and 08:45 UTC (Fig. 7), where we observe contrail properties and ambient atmospheric conditions at a flight level of ~12 km. Related parameters include N_{CAS}, NO, aspherical fraction, RHi, R_{eff}, and altitude. Close to 08:43:45 UTC, N_{CAS} and NO in the top panel are simultaneously enhanced (and exceed the contrail threshold values presented above) while R_{eff} (around the cloud top, Fig. 3) in the bottom panel decreases to values smaller than those of surrounding ice crystals. According to RHi in the range of 80% and 90% in the middle panel, we speculate that the rather spherical contrail particles which had formed near water saturation in the exhaust shortly after engine exit, hence at high ice supersaturations have not grown much and are now in the sublimating phase due to the unavailability of gas phase water for deposition. Therefore, they keep their original quasi spherical form and appear to be more spherical than the ice crystals in the surroundings. A prerequisite has to be assumed here that ice crystals develop the complexity at the surface after their initial formation and subsequent growth, and then the complexity disappears during sublimation, releasing a smooth and near spherical ice particle, similar with quasi spherical ice particles in convective clouds (Järvinen et al., 2016). Therefore, the reduced aspherical fraction (< 0.5) measured by CAS-DPOL in the subsaturated environment is also an evidence to indicate that contrail particles retain their quasi spherical form if they cannot grow by water uptake and sublimate. In addition, the fact that aspherical fraction in the surroundings reaches up to 1 and that R_{eff} does not exceed 20 µm (which is a relatively small value for natural ice crystals) could be an indication of (natural) ice particles inside dry layers close to cloud top sublimating next to young contrails that cannot grow larger due to low water vapour concentrations.~~

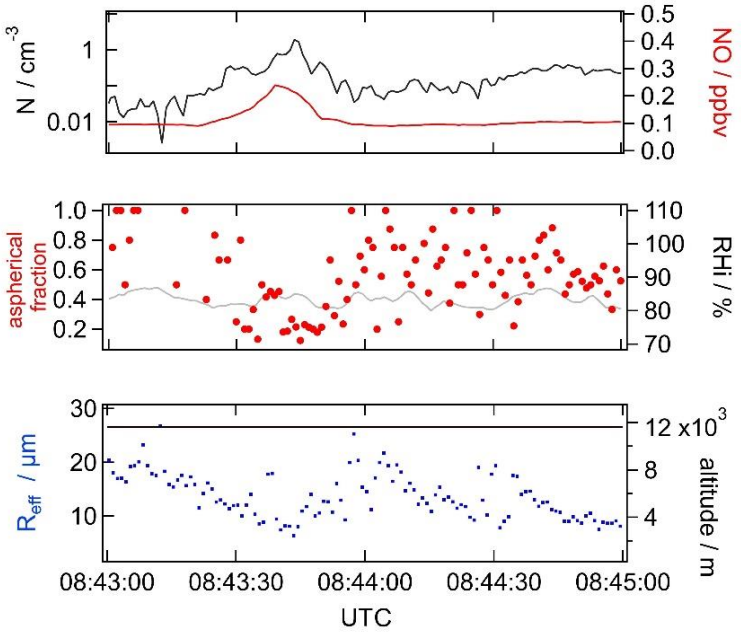

Figure 7: N, NO, aspherical fraction, RHi, R_{eff}, and altitude are shown for a short sequence of a dispersed contrail encounter between 08:43 and 08:45 UTC. NO and N are simultaneously referred to identify cirrus classification (top panel). An aspherical fraction value indicates whether the contrail ice particle has a quasi-spherical habit, and RHi is a criterion for saturation. With these two parameters, growth by water vapor uptake and sublimation of the particles are evaluated (middle panel). The size and location of contrails and surrounding cirrus clouds are presented by R_{eff} and altitude (bottom panel).

Here, we must note that the decreasing R_{eff} in the subsaturated environment from HALO are solely for this portion of the flight leg (compare to Fig. 2 for an approximate idea about the position of the aircraft to that time). This case study also emphasizes the importance of RHi accuracy, because ice crystal growth and sublimation are determined by ambient humidity conditions in the contrail cirrus regime.

3.2.2 Optical thickness and cloud top height

CiPS indicates a mean IOT of around 0.2 over the entire flight with a variability of ±0.1. Further, we order MSG/SEVIRI pixels according to the classification in Sect. 3.2, which is performed using the in situ data collected at given height levels in the cloud, and produce statistics for them separately. This attribution of course is not unambiguous since at different heights cloud properties the HALO flight track can be different. Following the discussion of the lidar data in Sect. 3.1, for instance the fall streaks of the contrails – containing larger crystals than the contrail cores – will also contribute to the contrail IOT and the upper layer cloud, whose origin is unclear – will add up to almost all measurements. Thus, it does not surprise that the median IOT for the three categories "natural cirrus", "contrail cirrus" and "contrails" are almost identical (Fig. 9a). The average IOT of natural cirrus and contrail cirrus are 0.21 and 0.24 respectively, and 0.15 for contrails. Furthermore, contrail pixels (which are much less in number than the other two categories) have a much smaller variability, with IOT always < ~0.3, while IOT for contrail cirrus and natural cirrus can be much higher. Fresh contrails are expected to have a higher IOT than contrail cirrus (see e.g. Unterstrasser and Gierens, 2010; Iwabuchi et al., 2012; Schumann et al., 2017) because of their large number of small ice crystals. Also, in the case of contrail formation within natural cirrus the increase in ice crystal numbers should lead to an increase in optical thickness right after formation. Comparing to literature, optical thickness of young contrails is estimated to be around 0.24 by Minnis et al. (2004), 0.240–0.274 by Iwabuchi et al. (2012), 0.216 (Bedka et al., 2013), 0.147±0.120 (Minnis et al., 2013), all from polar-orbiting instruments with better spatial resolutions. From MSG/SEVIRI, Vázquez-Navarro et al. (2015) show that the probability distribution function of "young" contrails (young with respect to the MSG/SEVIRI spatial

~~resolution: 30 min old at most after their first appearance in MSG/SEVIRI images) peaks at IOT < 0.2 and that IOT increases by ~ 0.1 after 3–5 h, leaving only either sublimating contrails pixels after 8 h or thicker cirrus pixels (IOT~0.4).~~

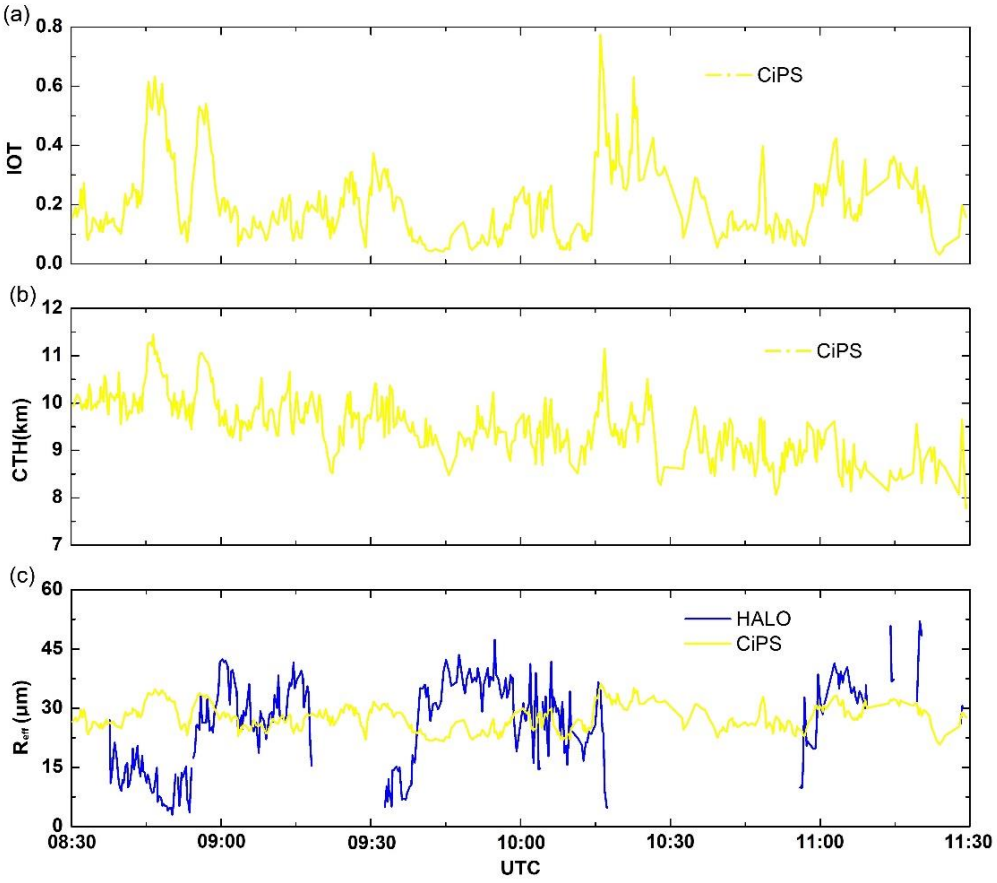

~~Figure 8: Temporal evolution of (a) IOT from CiPS, (b) CTH from CiPS and (c) R_{eff} from CiPS and from HALO at SEVIRI spatial resolution.~~

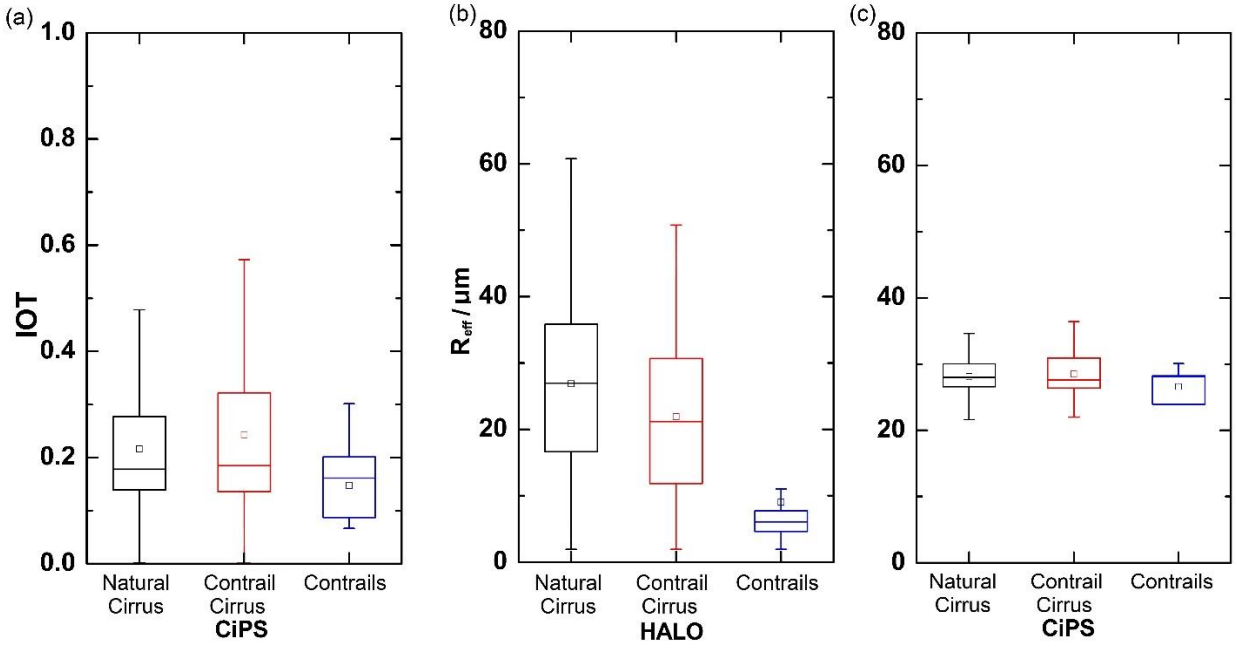

~~Figure 9: charts of (a) IOT from satellite observations by CiPS, (b) R_{eff} from HALO in situ measurements. Each bar contains the information of the maximum, minimum, interquartile range (25% percentile to 75% percentile), median (horizontal line) and mean (square)$_{eff}$.~~

~~Minnis et al. (2013) also show an increase of IOT during the temporal evolution of contrails to contrail cirrus (IOT=0.431, 3 times as large as the IOT of young contrails). In contrast, Unterstrasser and Gierens (2010) simulate a rapid decrease in optical thickness in the first 20 min after formation from values up to 0.7 to ~0.2, followed by a slow decrease of IOT with time. In Unterstrasser et al. (2017a) optical thickness also decreases fast during the first hour after contrail formation to IOT around 0.05-0.2, independently of synoptic properties, but afterwards cases of moderate updraft induce an increase in IOT again. In their compilation of contrail properties, Schumann et al. (2017) also indicate a decrease from IOT~1.0 to IOT~0.1 for contrails of age between 10 and 100 s, with IOT remaining almost constant up to 10,000 s (2 h 45 min). In simulations, Bock and Burkhardt (2016, their Fig. 7) show that ice crystal numbers can decrease while IWC increases and optical thickness – which is a vertically integrated quantity – does not have to necessarily decrease. Moreover, Bier et al. (2017, their Fig. 4g) show that in certain cases the mean optical thickness of a contrail cluster is first increasing. They also stress that there is a large variability in the temporal evolution that to a large extent depends on the synoptic situation (and not on microphysics). Thus, comparing to this literature, the contrails observed here (Sect. 3.2) are already relatively old and their IOT is comparable with that of contrail cirrus and natural cirrus, but due to the vertically integrated nature of passive satellite observations (and of IOT) differences between the classes are to some extent washed out. From the point of view of optical thickness, the entire cloud seems to be homogeneous without remarkable differences among the cloud types defined in Sect. 3.~~

~~With respect to CTH in Fig. 8b, CiPS results show that the cloud gradually decreased from the average height of 10.5 km at 08:30 UTC to ca. 8.5 km at 11:30 UTC, which present qualitatively the same pattern as lidar legs in Fig. 3 observed, although the CiPS values are lower by ca. 1.5 km in this case. The optically thicker cirrus cloud parts observed in the South (see above) are associated to a slightly higher altitude between 11.5 and 11.0 km, thus closer to the altitude observed by the lidar. Both remote sensing instruments, the lidar on HALO and MSG/SEVIRI, observe a sinking motion of the cloud that leads to its (partial) dissipation after the time period considered here (08:30–11:30 UTC), as can be seen in the IOT plots in Fig. 2.~~

3.2.~~3~~ 2 Effective radii

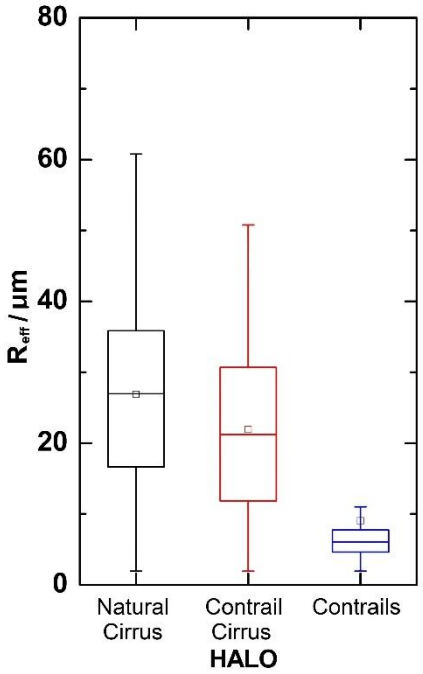

Figure 5: R_{eff} of natural cirrus, contrail cirrus and contrails from HALO in situ measurements. Each bar contains the information of the maximum, minimum, interquartile range (25% percentile to 75% percentile), median (horizontal line) and mean (square) R_{eff}.

~~In Fig. 8c a temporal sequence of the in situ and remote sensing R_{eff} from 08:30 to 11:30 UTC on 26 March 2014 is shown. As illustrated in Sect. 3.1, cirrus properties and characteristics can be very different at different heights and positions. In~~

particular, contrails seem to occur at certain levels, probably corresponding to a particular flight level, and at particular times. Furthermore, HALO was flying at different levels during the in situ legs such that different parts of the cloud could be probed: sometimes maybe the contrail core, sometimes ice crystals sedimenting out of the core, sometimes in even older contrails or in fresh ones. For instance, the first part of the first in situ leg at approx. 11.6 km seems to be most of the time between two cirrus cloud layers or at least in a thinner cloud layer where RHi is below saturation (also see in Fig. 6e, g) and ice crystals are sublimating. This part of the flight is characterised by small R_{eff} (between 5 and 25 µm) and many observations with high N (above 0.4 cm^{-3}) as well as NO (above 0.15 ppbv). In the second part of the first in situ leg, HALO descended to 11 km where many contrails were expected, at least around 52°N (see Fig. 6f) together with ice crystals sedimenting down from the upper layer or with ice crystals from natural or older contrail cirrus. This section is characterised by a mixture of small (3-20 µm) and high R_{eff} (up to 50 µm). The smaller R_{eff} are mainly at ca. 53.2°N, a little bit further North than the bulk of contrails observed in lidar leg 1 (up to 53.1°N) but in a location where some contrails maybe from the upper layer could be measured. RHi in this part of the first in situ leg is around 100%. The second in situ leg was flying first very close to cloud top, then down to 10.8 km and subsequently ascending in plateaus again to 11.2 km before ascending to 12.9 km. Very close to cloud top N is rather small (max. 0.3 cm^{-3}) and R_{eff} as well (mainly below 15 µm), indicating that only small particles are left here and/or that evaporation takes place in subsaturated air (RHi close to 90%). Hence, although in general natural ice nucleation especially close to cloud top is expected, this does not seem to be the case here at the time of the HALO flight where the cloud was already sinking (but natural ice crystals might have nucleated before or in the portion of the clouds with high RHi). At the second altitude level (10.8 km), in this leg R_{eff} is larger (around 40 µm) but N remains small and RHi is closer but usually below 100%. Afterwards, during the second altitude step in the ascent of HALO, RHi is well above 100% and R_{eff} is between 25 and 50 µm, with some N peaks above 0.3 cm^{-3}. This part of the flight path is between 52 and 54°N, i.e. in the Northern part of the race track where less contrails are observed by the lidar. In the last and highest plateau of the second in situ leg humidity is again close to 100%, R_{eff} become smaller (around 20 µm with large scattering) and many N peaks are observed. When HALO finally climbed to 12.9 km for the last lidar leg, R_{eff} and RHi sink very rapidly in the stratosphere. In the last in situ leg, only the first part is in cloud at 11 km. R_{eff} and RHi increase from cloud top (subsaturated) to this height, with supersaturation in the second part of the plateau. Towards the end of the plateau (at 51.5°N ca.) some very high N peaks are measured and R_{eff} is around 30 µm. Finally, HALO dived below the ice cloud. In general, as Fig. 6e and Fig. 5b show, the RHi for these 3 in situ legs are both below and above 100%, i.e. in subsaturation and supersaturation. In particular, many ice crystals are found in air with RHi<100%.

Considering the entire flight and separating R_{eff} measurements according to our classification enables us to study the statistical properties of the ice crystal sizes. From Fig. 5, contrail cirrus R_{eff} probed from airborne instruments are smaller than those of natural cirrus, with an average R_{eff} of about 22 µm. The natural cirrus has an average R_{eff} of 27 µm, which is at the lower end of the particle size distributions observed in natural cirrus (Schröder et al., 2000). The mean radii of contrail cirrus or contrails from in situ measurements is 18% smaller than that of natural cirrus. From contrails to contrail cirrus, the mean and medium values of particle size **R_{eff}** mainly show an increasing tendency by an average difference of 13 µm (144%) for this situation. Despite the uncertainty of probed particle sizes, the radii of natural cirrus reached up to 60 µm, while the majority of maximal R_{eff} of contrail cirrus topped at 53 µm, in agreement with findings of Voigt et al. (2017). This is consistent with the physical picture that contrails form initially as small particles and increase in size by water vapor uptake in ambient ice supersaturated air, when air is supersaturated. If no supersaturation is present, contrails dissipate and cannot evolve into contrail cirrus. HoweverStill, contrail cirrus as well as natural cirrus can consist of sublimating particles when air becomes subsaturated (Kübbeler et al., 2011).

Finally, we jointly assess radii variations of natural cirrus and adjacent contrail cirrus from CiPS with simultaneous HALO measurements for this NAR case. Here, HALO in situ R_{eff} is shown as an average over each SEVIRI pixel. However, satellite observations have contributions from the entire cloud column, and in situ measurements are solely for one certain flight level,

~~and in this case, contrails are embedded in ice cloud layers (Fig. 3) that probably have different microphysical and optical properties, consisting either of natural or contrail cirrus. In fact, we have seen above that a difference in R_{eff} is present among the three cloud classes. These reasons hinder a one-to-one comparison between in situ and spaceborne measurements. Nevertheless, we want to investigate whether the thermal satellite observations of CiPS are able to collect some characteristics of the contrails and contrail cirrus. The temporal variability of CiPS R_{eff} along the flight path is smaller than that of simultaneous in situ R_{eff} averaged over the MSG/SEVIRI pixels (Fig. 8c). R_{eff} from the thermal CiPS retrieval varies around ~30 µm along the entire flight path and no clear correspondence is observed. Nevertheless, mean values (Fig.9c) of CiPS are not far away from the in situ values and the R_{eff} for contrails shows a smaller range than those for the other two cloud classes. Of course, this might also be due to the smaller number of contrail samples.~~

In sum, satellite, lidar and in situ measurements give combined evidence for an ideal case of a contrail cirrus outbreak with a high fraction of contrails and contrail cirrus embedded in natural cirrus. In the following, we investigate its radiative impact.

4 Radiative effects of contrail cirrus and natural cirrus

Here, we develop a new estimation method for TOA net instantaneous cirrus RF that relies on satellite and in situ observations. TOA irradiance ~~with contrail cirrusnatural cirrus~~of the contrail cirrus outbreak can be observed, but the comparable situation without ice clouds has to be obtained from another source, e.g. from the surroundings (like e.g. in Vázquez-Navarro et al., 2015 for contrails) or from model simulations (Haywood et al., 2009 for contrail cirrus). The instantaneous net RF at TOA is the change of the total irradiation under a situation with cirrus minus the irradiances in the same situation without cirrus. In fact, the SW component of the cirrus RF $RF_{SW_{TOA}}$ ~~of the cirrus~~ can be diagnosed as

$$RF_{SW_{TOA}} = SW_{\uparrow no\ cirrus} - SW_{\uparrow cirrus}\ . \quad (3)$$

Notice that $SW_{\uparrow cirrus}$ corresponds to the RSR that can be observed by the satellite. Similarly, the LW RF $RF_{LW_{TOA}}$ can be diagnosed from

$$RF_{LW_{TOA}} = LW_{\uparrow no\ cirrus} - LW_{\uparrow cirrus}\ . \quad (4)$$

Again, the cirrus term $LW_{\uparrow cirrus}$ in Eq. (4) corresponds to the OLR that can be computed from MSG ~~using the RRUMS algorithm~~. The net cirrus RF $RF_{NET_{TOA}}$ is defined as

$$RF_{NET_{TOA}} = RF_{SW_{TOA}} + RF_{LW_{TOA}}\ . \quad (5)$$

However, the two values (TOA irradiance with cirrus and without cirrus) are similar in size since ~~contrails and~~ contrail cirrus represent a small perturbation. In fact, both in Vázquez-Navarro et. (2015) and Haywood et al. (2009) taking the difference between the cirrus contaminated and the cirrus-free irradiances leads also to negative values of RF in the thermal range (OLR with ice clouds is larger than OLR without ice clouds) or to positive RF in the solar range (RSR with ice clouds is smaller than RSR without ice clouds). This is ~~of course~~ unphysical and we would like to avoid it. To this end, in Sect. 4. 1 ~~a new method~~ we developed a new method based on RTM calculations exploiting airborne measurements, satellite observations and ERA5 model atmospheric data that produces TOA irradiance ~~that is~~ fully consistent for both cirrus and cirrus-free regions. ~~The combination of these datasets however does not allow to take care of the full vertical and spatial variability of clouds, as they can be observed for instance in the WALES data (Fig. 3), and assumptions have to be introduced.~~ So finally, to ensure that TOA irradiance calculated this way is realistic, we compare our RTM simulations of RSR and OLR for the cirrus contaminated case with satellite observations of RSR and OLR from RRUMS at pixel level. An additional comparison on a 3x3 pixel scale with the more accurate GERB products is performed to assess the RRUMS accuracy on this particular day (S4 and Fig. 3). ~~We don't apply GERB directly since we want to evaluate RF along the HALO path and GERB is available for 3x3 SEVIRI pixel areas.~~

~~4.1 Evaluation of RRUMS with GERB~~

~~To evaluate TOA irradiance from RRUMS during this day, we compare GERB products (RSR_G and OLR_G), comprising 3x3 pixels of MSG/SEVIRI, with RRUMS results along the HALO flight trajectory. Notably, different cirrus classifications have the same TOA value from GERB products and RRUMS results since the temporal/spatial resolution of the in situ data is much higher than that of SEVIRI. We first remove 7.5% bright errors and 1.3% cold bias of the GERB irradiances in the solar and thermal range (Clerbaux et al., 2009) to build new revised GERB datasets. We then calculate the 3x3 pixel mean values of RRUMs results. The corresponding RSR_R correlates well with RSR from GERB (RSR_G: correlation coefficient CC=0.72), but RRUMS tends to overestimate GERB (Fig. 10a).~~

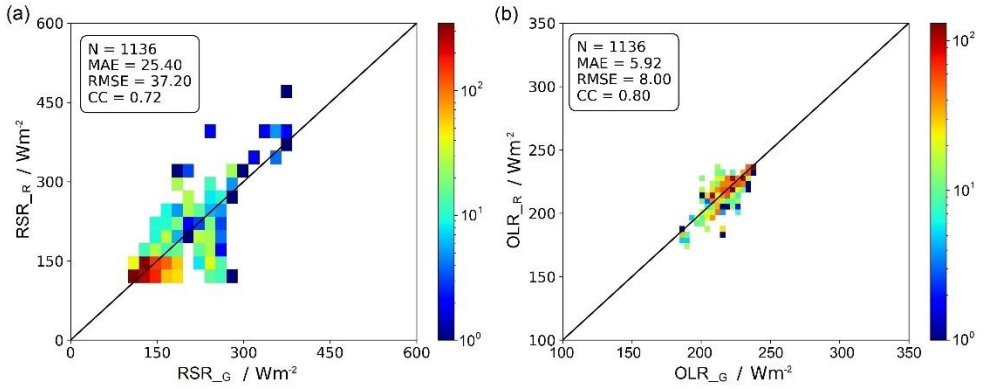

~~**Figure 10: Comparison of TOA (a) RSR and (b) OLR from RRUMS algorithm results (RSR_R, OLR_R) and revised GERB datasets (RSR_G, OLR_G) (3×3 SEVIRI pixels) along the HALO flight on 26 March 2014. The MAE, RMSE and CC are used as metrics.**~~

~~In terms of OLR, the agreement is good, with a mean absolute error around 6 W m^{-2} and a correlation coefficient of 0.80 for OLR_R and OLR_G (Fig. 10b).~~

4.~~2~~ 1 RTM simulations of TOA irradiance ~~along the HALO flight path~~

In this section we illustrate the new method used to derive instantaneous cirrus RF and show that it compares well to observations of RSR and OLR by RRUMS ~~(see introduction of this section)~~. In particular, we explain a 2-step method to compute both cirrus-free and cirrus influenced TOA irradiances. First, an atmosphere is set up as input to the RTM that contains a realistic representation of the situation observed including in particular all clouds. Then in a second step the ice clouds are removed, for which the RF is to be computed. This provides the cirrus-free reference TOA irradiance for the calculation of cirrus RF. ~~This means that the RTM calculations are performed twice, once for the conditions unaffected by contrails and contrail cirrus at the flight level and once with contrail and contrail cirrus.~~ The basic setup of the RTM is described in Sect. 2.3. Every RTM calculation needs an atmospheric state as input. This is in part obtained from ECMWF ERA5 reanalysis data (Hersbach et al., 2020). All 137 model levels are used. The horizontal and temporal resolution are 0.25° × 0.25° and 1 h. We derived temperature profiles, logarithm of surface pressure, specific humidity, ozone mass mixing ratio, and land or sea mask. Densities of gaseous water (H_2O) and ozone (O_3) are derived from specific humidity and O_3 mass mixing ratio. CO_2 is set to ~~have~~ a volume mixing ratio of 400 ppm. Vertical profiles of liquid clouds are also extracted from ERA5 data ~~as well since it is difficult to determine their presence and properties from SEVIRI when they have a cirrus cloud on top~~. We choose vertical profiles close~~st~~ to the HALO flight time, i.e. with a time difference of 30 min at most between model and in situ measurements. We rely on the fact that reanalysis data should provide a realistic description of cloud properties and cloud positions, but we accept that this procedure might cause small temporal shifts such that observations close to cloud edges might~~are~~ not be represented in an optimal way through the model data. However, we refrain from interpolating cloud properties in time since also this procedure would create artificial clouds that do not exist in reality, especially in locations where no cloud is present at a given time but it is there at the next time. For liquid clouds, the parameterization by Bugliaro et al. (2011, 2022) is~~are~~ applied for creating R_{eff} profiles ~~and optical properties from model output~~using IWC and temperature from ERA5. ~~Of course,~~

their presence and properties are crucial especially to RSR and the situation encountered here is particularly challenging since the HALO track (Fig. 2) runs almost parallel and sometimes very close to the edge of a low level (yellowish in the RGBs) cloud field. The solar zenith angle corresponds to synchronous SEVIRI observations. Besides, the albedo of ocean is parameterized following Cox and Munk (1954a, b) and Nakajima and Tanaka (1983), especially involving the wind speed from ERA5. For ice clouds, another procedure is applied. Since SEVIRI observations with CiPS are able to account for the entire cirrus cloud layers but are only dependent on thermal channels and not affected by low lying clouds (Strandgren et al., 2017b), SEVIRI provides accurate ice cloud properties (IOT) that can be used in the RTM.

The representation of cirrus at the flight level is complemented by adding their R_{eff} from in situ measurements, CTH and cirrus bottom height (CBH) from lidar legs, as well as CiPS IOT into libRadtran in the way described in the next lines. This way we simulated a vertically homogeneous ice cloud with the correct IOT obtained by CiPS. We assumed IOT to be constant over an entire SEVIRI pixel while R_{eff} varies changes according to in situ information (however at the single altitude levels probed by HALO). Since the RTM needs IWC as input, we determine it from IOT. First, Extinction *Ext* for IWC = 1 g m^{-3} (i.e. extinction in km^{-1}/ (1 g m^{-3})) for each measurement is first interpolated to the given in situ R_{eff} with the parameterisation of optical properties of Baum et al. (2011) for rough aggregates. The selection of this shape for all cloud types is motivated by the fact that each cloud column, even those containing contrails, encompass ice crystals with various temporal evolution, e.g. young small – probably round, ice particles in contrail cores together with larger sedimenting ice crystals in the fall streaks with different shapes or with evaporating ice crystals – in part still large in size, in undersaturated subsaturated air that are starting to lose asphericity or maybe even natural ice crystals produced by homogenous nucleation with unknown shape. To avoid an additional arbitrary choice with respect to ice particle shape we decided to keep the method as simple as possible and selected this shape (rough aggregates) as e.g. for the MODIS optical property products Collection 6. Note the parametrization of this shape only covers R_{eff} from 5 to 60 µm, which results in the inexecutable RTM calculations for larger or smaller ice crystals. 20 cases in total are removed but have a negligible effect on the estimation of radiative effects as R_{eff} of natural cirrus and contrail cirrus always fall in the range where RTM could simulate as indicated in Fig.9. The IWC for each measurement of R_{eff} corresponding to a vertically homogeneous ice cloud with given IOT is derived using the following equation:

$$\mathrm{IWC} = \frac{IOT}{Ext*(CTH-CBH)} \quad (6)$$

CTH and CBH are obtained from the lidar legs since they seem to vary only slowly with time and space (Fig. 3). Thus, this IWC is used to simulate a homogeneous ice cloud layer between CBH and CTH and corresponds to the IOT observed by CiPS. Finally, every in situ measurements of R_{eff} is are assigned to a cloud class (Sect. 3.2.1) and a collocated IOT from CiPS as well as the ERA5 properties listed above for temperature, gas and liquid water clouds. With this atmospheric setup, TOA irradiances are computed and represent the cirrus contaminated RSR and OLR. Then, the ice clouds only are removed from the input of the RTM and other calculations are performed to compute cirrus-free irradiances. Both together are then inserted in Eqs. (3)-(5) to compute the instantaneous net RF of the cirrus cloud under consideration.

The RSR and OLR values influenced by contrails, contrail cirrus and natural cirrus as obtained from libRadtran simulations (RSR_L and OLR_L) and compared with RRUMS algorithm outputs (RSR_R and OLR_R) along the flight path of HALO are presented in Fig. ure 6. The two methods agree quite well, but the RTM calculations tend to underestimate large RSR values, probably due to too thin, missing or even mismatched liquid water clouds that are taken from ERA5. Uncertainties in ice cloud properties cannot have such a large effect on RSR since their optical thickness is very low around 0.2 (Sect. 3.2.2). Furthermore, a smallerslight overestimation of RSR by the RTM compared to RRUMS during leg 2 (9:30-10:30 UTC) is also observed for the smallest RSR values below 150 W m^{-2}, related to an underestimation the bias of estimated ocean albedo but improved by the application of wind speedduring this time. For OLR, the agreement between the two datasets is good, with both slight (< 10 W m^{-2}) overestimations and underestimations.

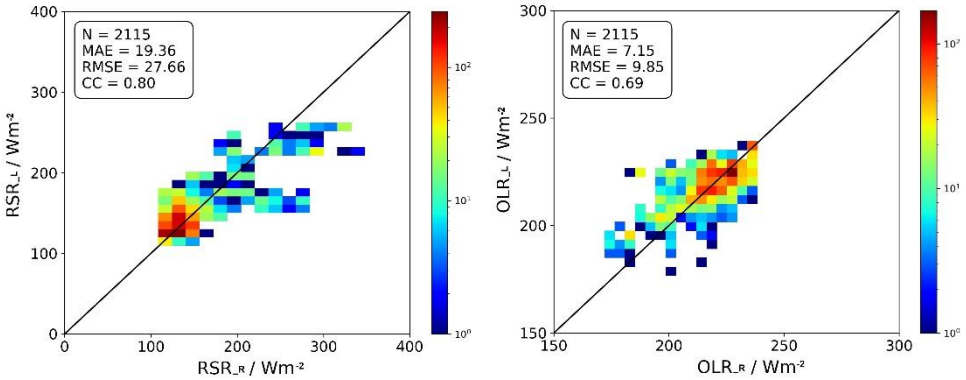

Figure 6: Comparison of TOA (a) RSR and (b) OLR from our RTM simulations (RSR $_L$, OLR $_L$) for probed ice particles and RRUMS algorithm results (RSR $_R$, OLR $_R$) for single SEVIRI pixel along the HALO flight on 26 March 2014. The mean absolute error (MAE), root mean square error (RMSE) and correlation coefficient (CC) are used as metrics.

The RTM based TOA radiation estimation method provides a good representation of the real atmosphere and will be used to determine RF of the ice clouds ~~probed during this flight~~ in the following section. ~~However, to reduce the impact of the incorrect consideration of low-level clouds mentioned above, an additional filtering is used. We consider the ratio of the RMSE value of RSR from RRUMS against GERB (Sect. 4.1) divided by the mean RRUMS RSR (ratio=0.19) as a measure for the uncertainty of RRUMS and neglect all RTM simulations that differ by more than this fraction from RRUMS. This way, 1724, 795 and 19 points for natural cirrus, contrail cirrus and contrails are left, with 191, 79 and 0 points filtered out for each category.~~

~~4.3 TOA radiative forcing during the HALO flight~~

~~We evaluate RF of probed contrail cirrus and natural cirrus along the HALO flight route using Eqs. (3) (5). TOA cirrus-free RSR and OLR along the flight path of HALO are calculated by excluding the ice cloud layer at the flight level from the radiative transfer calculations. Figure 12a indicates the patterns of TOA RF for natural cirrus, contrail cirrus and contrails (around the flight level) versus time. Strikingly, natural cirrus and contrail cirrus show very similar patterns in SW, LW and net RF due to their similarity in IOT and despite small differences in R_{eff}. Both positive and negative net RF values are present with largest variability before 9:45 UTC. This is due to the peaks of higher IOT up to approx. 0.6 (Fig. 8) that induce a higher reflection of solar radiation and also make the cloud less transparent to thermal radiation thus increasing both its SW and LW forcing. However, in case of an ice cloud on top of a low-level cloud, especially SW RF is usually reduced, since the increase of reflection is then less pronounced. From 9:30 to 10 UTC net RF is mainly positive and after 10 UTC a tendency to negative net RF is observed. The larger values of RF around 10:15 UTC are again caused by the increase in IOT. After 10:15 UTC HALO was then performing the third lidar leg (Fig. 6) such that they are not included in this calculation. Also, the few contrails show either slightly positive (< 5 W m^{-2}) values or negative values (> −2 W m^{-2}). Over the entire flight, CTH is sinking such that earlier observations should correspond to slightly higher OLR (cloud top is sinking only slowly, Fig. 3) and thus larger LW RF since sea surface temperature, that largely affects cloud-free thermal irradiances, is staying almost constant over the day. However, this effect is modulated by cirrus IOT and by the presence of low-level clouds (as explained above).**

As depicted in Fig. 12b, the average natural cirrus RF in Fig. 12a are 7.7 and −7.1 W m^{-2} in the LW and SW, respectively, resulting in a net forcing of 0.6 W m^{-2}. Contrail cirrus net RF of 1.6 W m^{-2} is usually larger than that of natural cirrus, with the LW and SW RF of 8.8 and -7.2 W m^{-2}. As for contrails, their RF in the LW and SW are 6.2 and -5.8 W m^{-2}, with a net value of 0.4 W m^{-2}. Thus, RF from contrail cirrus is a factor of 4 higher than RF for contrails, which is mainly due in these RTM simulations to the lower IOT of contrails (Fig. 9a).

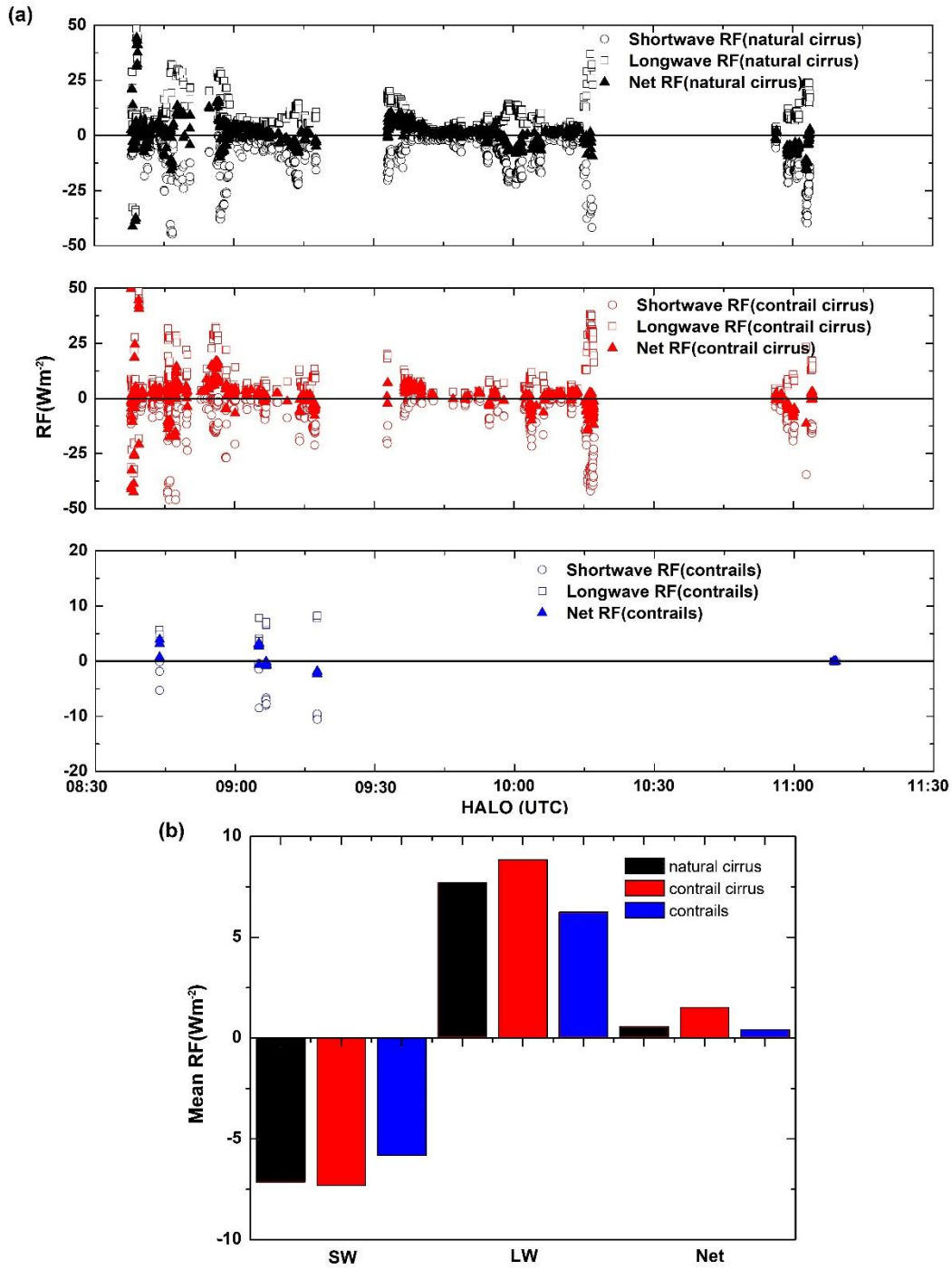

~~**Figure 12: (a) TOA LW, SW and net RF of natural cirrus, contrail cirrus and contrails from our RTM simulations for HALO probed ice particles along the HALO flight path over NAR on 26 March 2014, and(b) corresponding mean values.**~~

4.~~4~~ 2 Diurnal cycle of TOA RF of ~~ice clouds in the area of the HALO flight~~the contrail cirrus outbreak

In Sect. 4.~~3~~ 1 we presented TOA RF for each waypoint of the probed cirrus. In order to examine ~~whether~~ microphysical properties and radiative effects of ~~cirrus~~ the contrail cirrus outbreak detected ~~during the HALO flight are representative of~~in this area and ~~this time and~~to analyse the corresponding temporal variation, we present the regional cirrus cover (CC), average cirrus IOT and CTH (all three quantities from CiPS), ~~ambient atmospheric conditions vertical velocity and RHi from ERA5)~~ as well as mean TOA SW, LW and net RF in an area of 36 × 51 pixels (~16500 km^2, the red area in Fig. 2) near the HALO flight track, characteristic for contrail cirrus and cirrus as shown in Sect. 3. This area extends mostly ~~West~~ east of the HALO flight and thus ~~containing the eastern edge of the ridge cloud or at least~~contains the contrails or ~~/~~contrail cirrus formed directly ~~East~~ east of the ridge cloud. ~~In the East the red area is already at 8 UTC partly free of ice clouds. The classification of ice clouds into different classes as in Sect. 3.2.1 is of course not available such that we~~ We consider here all ice clouds in the

region with high aviation impact. ~~Considering the satellite observations in Fig. 2, we suppose that the ice cloud field is impacted by aviation in a similar way as the HALO flight path.~~

RF in this section is at the SEVIRI resolution, and calculated using CTH, IOT from CiPS, R_{eff} from in situ mean values of all cirrus, ~~and CBH estimated from CiPS~~ and cloud thickness from WALES assuming the latter doesn't change in the area with the same procedure presented in Sect. 4.1 based on the RTM libRadtran. ~~Figure 13a, b, and d show the regional CC, average IOT and CTH from CiPS, and mean TOA SW, LW and net RF for an area of 36 × 51 pixels (~16500 km^2) computed with libRadtran. Fig. 13c represents the mean vertical velocity and mean RHi within the pressure difference of ± 25hPa around 225 hPa (the average pressure height of HALO) in the area of interest.~~

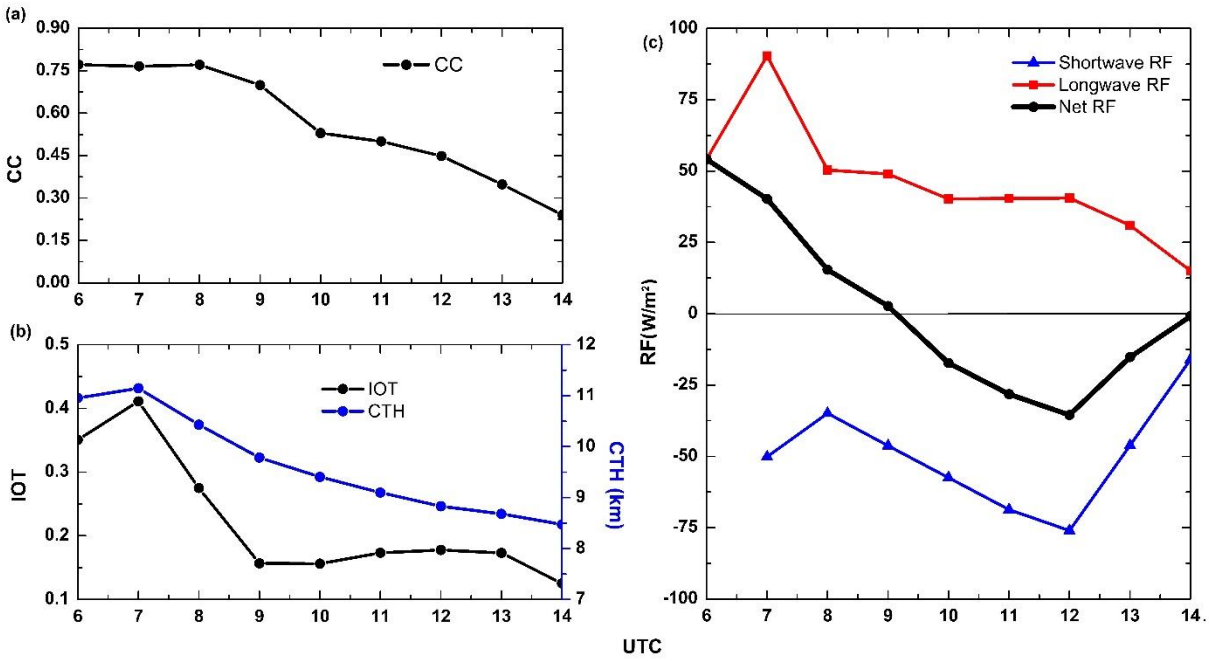

Figure 7: The variations of (a) CC, (b) mean IOT and mean CTH, ~~(c) mean vertical velocity and RHi within the pressure difference of 25hPa around 225hPa,~~ and (~~d~~c) SW, LW and net RF within the area indicated by a red box in Fig. 2.

In Fig. 7a, we observe that CC gradually decreases from 0.77 at ~~08~~ 06 UTC to 0.25 at 14 UTC ~~(this can be observed in Fig. 2 until UTC) with the steepest decrease until 14 UTC (CC=0.25) and a slower decrease from 14 to 18 UTC~~. The positive vertical velocity from ERA5 around that region ~~before 15:00 UTC shown in Fig.~~ implies the local downward motion of airmass to warmer temperature layers and the CTH also decreases. ~~Similar to Sect. 3.,~~ IOT in Fig. 7b decreases between 0~~7~~8:00 (0.41~~28~~) and 10:00 UTC (0.15), then slowly increases until 12 UTC (0.17), then falls to 0.12. CTH decreases during the day and is thus consistent with both the observations of HALO (Fig. 3) and the downward motion ~~(Fig. 13c)~~. ~~Mean CTH values over the red area are similar to those along the HALO flight track (Fig. 8).~~ Since an underestimation of CTH by CiPS with respect to WALES (Fig. 3) is observed there, we ~~might~~ assume that CTH is also underestimated by CiPS in this area.

~~Similar to and at some time unlike the situation along the HALO path,~~ Mean net RF over this area in this synoptic situation is positive in the early morning until 9 UTC with the maximum of net RF is at 7 UTC when the sun has risen. Hence the contrail cirrus outbreak is warming during night and early morning hours. ~~and in the afternoon UTCOf course, after 14 UTC CC is already very low such that the mean RF values also tend to approach 0 W m^{-2}.~~ After 9 UTC, the forcing becomes negative. More explicitly, from around 9 to 14 UTC the net RF is negative and thus this contrail cirrus outbreak tends to cool during daytime. The strongest cooling is observed at 12 UTC. ~~The strongest cooling is at 12 UTC and the maximum of net RF (warming) is at :00 UTC. From 9 to 1 UTC net RF is mainly negative and thus this ice clouds with the contrails and contrail cirrus tend to cool during daytime.~~ Notice however that the possible underestimation of CTH by CiPS in this area would result in the general underestimation of the LW RF results since a lower CTH reduces the contrast to the cirrus-free OLR. In turn, this would further shift cirrus net RF towards cooling.

5 Summary and conclusions

This study provides a detailed investigation of an ideal ~~situation with~~ contrail cirrus ~~and natural cirrus~~outbreak event ~~that combines~~with airborne in situ probes, airborne lidar measurements and geostationary satellite observations~~. We have tackled aspects related to microphysical properties and radiative effects through~~ using ~~one~~ a case study focusing on the NAR on 26 March 2014 during the ML-CIRRUS experiment. We choose this contrail cirrus outbreak case because of the large contrail cirrus coverage and high air traffic density. As flight operation in all altitudes is not easily granted due to the high air traffic load in the NAR, the data presented here is also rare and unique in the sense that HALO was able operate and acquire in-flight measurements of contrail cirrus perpendicular to the flight tracks of the NAR. From satellite remote sensing, few low-level water clouds and the relatively homogeneous oceanic background increases the sensitivity to retrieve cirrus properties. On the morning of that day the HALO research aircraft flew for three hours in or above cirrus clouds, contrail cirrus and ~~with~~ contrails ~~that were formed probably some hours before~~. Various contrails with related fall streaks ~~can be~~have been identified in airborne lidar backscatter ~~images and~~data which merge to a larger cloud with a vertical extent of ~~approx.~~ 2 km that dissipates with time. High resolution RGBs and BTDs from MSG/SEVIRI also reveal the presence of various line shaped structures that represent ~~persistent~~ contrails. Simultaneous airborne humidity measurements from AIMS show ~~ice subsaturated regions in large parts of the cloud, but also large supersaturations (~~RHi between 80% and~~>~~ ~~140~~120%, in line with lidar observations indicating a region~~) that would also support natural ice cloud formation events~~. ~~We assume that~~where contrails formed, evolved and merged ~~and that homogeneous nucleation of~~with natural ~~ice particles followed~~cirrus.

~~Primarily, a "contrails, contrail cirrus and natural cirrus" database has been set up with a novel method from airborne measurements that~~ We identify~~ies~~ aircraft plumes ~~from~~ using peaks in NO ~~trace gas measurements~~data with an approach that takes care of the variable NO background, and ~~differentiate~~contrast~~s~~ contrails ~~from~~ and contrail cirrus on the basis of measured ice number concentrations ~~at the flight level. Along the HALO flight path, MSG measured an average IOT for the cloud layers containing the natural cirrus, contrail cirrus and contrails (classified from in situ) of 0.21, 0.24 and 0.15, respectively. till a difference in R_{eff} inside the cloud is present.~~ The mean radii of contrails or contrail cirrus ~~from in situ measurements~~ is about 18% smaller than that of natural cirrus, suggesting a self-stabilizing mechanism of smaller contrail cirrus particle sizes surviving due to higher ice number concentrations in contrail cirrus compared to natural cirrus. ~~As for microphysical variations from contrails to contrail cirrus,~~ Ice particle sizes increase by about 144~~114~~% during the transition from contrail to contrail cirrus by deposition of ~~ambient~~ water vapor in regions with ice supersaturation. ~~In fact, RHi correlates with effective ice crystal size, with smaller R_{eff} for RHi close to or below saturation and larger R_{eff} in ice supersaturated air. As far as MSG observations of R_{eff} in the thermal range with the CiPS algorithm are concerned, mean values are close to the in situ values and the R_{eff} derived from the size distribution of contrails shows a smaller range than those for the other two cloud classes. However, it seems that due to the sensitivity of the thermal algorithm and the complicated vertical structure of the cloud, CiPS is not able to reliably identify the presence of contrails (with smaller R_{eff}) in the cloud layer.~~ Thus, combined evidence from satellite and aircraft data suggest the presence of an ideal contrail cirrus outbreak event.

For purpose of obtaining accurate radiative effects of contrail cirrus and natural cirrus ~~and contrails~~, a new TOA RSR and OLR estimation method is developed, which is based on detailed RTM calculations and exploits in situ measurements, satellite observations and ERA5 model atmospheric data. Using IOT from MSG/SEVIRI (CiPS), R_{eff} from in situ, cloud top and bottom height from the lidar, and gas, temperature and liquid water cloud profiles from ERA5, an input atmospheric state for the RTM has been defined that enables to compute RSR and OLR that compare well to MSG measurements (RRUMS). When the ice cloud layer ~~(contrails, contrail cirrus, and natural cirrus)~~ is removed from the RTM input, RSR and OLR for cirrus-free conditions can be computed that are consistent with the corresponding cirrus ~~contaminated quantities~~data. ~~This way, RF for the three cloud classes identified in situ can be computed. Contrail cirrus net RF is larger by a factor of 4 with respect to contrails RF and is larger than that of natural cirrus as a whole. However, we have to note that few individual contrails observed here have a smaller RF.~~

For a larger area of 36 × 51 SEVIRI pixels adjacent to the HALO flight path, the diurnal cycle of ~~cirrus (all types together)~~the contrail cirrus outbreak was computed. RF of cirrus is associated with the changes of cirrus coverage~~CC~~, CTH and IOT. Here, we find a ~~the~~ positive net RF of the contrail cirrus outbreak region in the early morning, and the contrail cirrus outbreak warms at TOA ~~lasts~~ till 9 UTC ~~and~~. ~~then~~ Then during daytime the mean net RF of ~~cirrus, contrail and contrail cirrus~~ the contrail cirrus outbreak becomes negative, and the contrail cirrus outbreak cools~~leads to a reduced energy input into the atmosphere and to a cooling effect~~. In the long-term observations or hourly resolved simulations of ~~the~~ contrail cirrus coverage and RF in the NAR ~~in 2019~~, Graf and Schumann (2012), Duda et al. (2013), and Vázquez-Navarro et al. (2015) ~~Teoh at al. (2022)~~ also find the contrail coverage is important and that a high variability of the contrail impact exhibits. These studies indicate that contrail cirrus warm during the night, while a larger variability in contrail cirrus RF exists during the day. Teoh et al. (2022a, b) show that ~~any cases of contrails and~~ contrail cirrus often cool~~sing~~ during daytime and that the cooling depends on many parameters including solar zenith angle and the surface albedo. For some cases with low clouds Teoh et al. (2022a, b) also find warming contrail cirrus during the day. In the absence of sunlight during night time however, ~~while~~ contrail cirrus ~~of course~~ warms the atmosphere ~~during nighttime~~. ~~We present only observations of one day in one particular synoptic situation.~~ Here we use a new method to derive the RF of contrail cirrus and cirrus and we test it using in-situ and lidar observations in a contrail cirrus outbreak situation. A following study will aim at applying the method to a broader data set to investigate the radiative effects of cirrus and contrail cirrus using RTM simulations involving CTH and IOT from satellite, R_{eff} from in situ values, and CBH and cloud thickness from lidar. ~~It is known that synoptic conditions have a large impact of contrail cirrus properties (Bier et al., 2017). Nonetheless, according to Muhlbauer et al. (2014) almost half of the cirrus cloud occurrences close to the Atmospheric Radiation Measurement Southern Great Plains (SGP) site in Oklahoma during the Department of Energy Small Particles in Cirrus (SPARTICUS) campaign was explained by three distinct synoptic regimes, one of them being upper level ridges. Assuming that this is true for cirrus clouds in European mid-latitudes as well (despite the fact that SGP is located over land and close to 36°N, which corresponds to the southern tip of the Iberic Peninsula in Europe and thus has a warmer climate than the NAR) and together with the fact that air traffic to and from the US takes place every day, the situation encountered here might take place often in this area and our numbers could be representative for such conditions. In contrast, since frontal clouds are expected to be optically thicker, contrails and contrail cirrus formed in connection with such systems are probably not comparable to the one presented here.~~

This work is valuable for identifying contrails, contrail cirrus and natural cirrus from different platforms, estimating TOA RF from satellite data, assessing microphysical properties and climate impacts of anthropogenic cirrus and natural cirrus, and can help to formulate~~ing~~ appropriate contrail mitigation options.

Data availability

Flight measurements are available at the HALO data base at https://halo-db.pa.op.dlr.de/. The SEVIRI data are provided by EUMETSAT (European Organisation for the Exploitation of Meteorological Satellites) and the modelled atmospheric profiles are obtained from ECMWF (European Centre for Medium-Range Weather Forecasts). The GERB data could be accessed from EUMETSAT (GERB international team).

Author contributions

Z.W. conducted the analysis and wrote the manuscript. L.B. advised the study and provided feedbacks on the manuscript. L.B., M.W., and G.D. plotted Fig. 1 & 2, 3, and S1. C.V. coordinated the ML-CIRRUS mission and L.B. and T. J. contributed to the flight planning. T.J., R.H., H.Z., M.W., S.G., S.Ka., and C.V. participated in the flight measurements. G.D. wrote the description of WALES datasets. Z.W., L.B., T.J., R.H., H.Z., and C.V. discussed the cirrus classification. U.B. helped with the interpretation of the cirrus cloud conditions and evolution. All authors contributed to and commented on the manuscript.

Competing interests. The authors declare that they have no conflict of interest.

Acknowledgements

We thank the DLR flight crews for excellent flight operations and EUMETSAT and ECMWF for providing the MSG/SEVIRI observations and modelled atmospheric data, as well as Royal Meteorological Institute of Belgium (RMIB) in the team of the GERB system for supplying GERB-like data. We thank Bernhard Mayer and team for developing the LibRadtran model. We are grateful for the air traffic dataset provided by M3 and NATS and edited by Ulrich Schumann. This work is supported by the German Research Foundation within SPP-1294 HALO (grant no VO1504/6-1 and VO1504/7-1) and TRR 301 (Project ID 428312742). Z.W is supported by the DLR (Deutsches Zentrum für Luft- und Raumfahrt) / DAAD (Deutscher Akademischer Austauschdienst) Research Fellowships - Doctoral Studies in Germany, 2020. T.J. also thanks the DLR project H2CONTRAIL. We thank Manuel Gutleben for interesting comments that helped improve the paper.

References

Atlas, D., Wang, Z., and Duda, D. P.: Contrails to Cirrus—Morphology, Microphysics, and Radiative Properties, Journal of Applied Meteorology and Climatology, 45, 5-19, 10.1175/JAM2325.1, 2006.

Baum, B. A., Yang, P., Heymsfield, A. J., Schmitt, C. G., Xie, Y., Bansemer, A., Hu, Y.-X., and Zhang, Z.: Improvements in Shortwave Bulk Scattering and Absorption Models for the Remote Sensing of Ice Clouds, Journal of Applied Meteorology and Climatology, 50, 1037-1056, 10.1175/2010JAMC2608.1, 2011.

Baumgardner, D., and Gandrud, B.: A comparison of the microphysical and optical properties of particles in an aircraft contrail and mountain wave cloud, Geophysical Research Letters, 25, 1129-1132, https://doi.org/10.1029/98GL00035, 1998.

Baumgardner, D., Brenguier, J. L., Bucholtz, A., Coe, H., DeMott, P., Garrett, T. J., Gayet, J. F., Hermann, M., Heymsfield, A., Korolev, A., Krämer, M., Petzold, A., Strapp, W., Pilewskie, P., Taylor, J., Twohy, C., Wendisch, M., Bachalo, W., and Chuang, P.: Airborne instruments to measure atmospheric aerosol particles, clouds and radiation: A cook's tour of mature and emerging technology, Atmospheric Research, 102, 10-29, https://doi.org/10.1016/j.atmosres.2011.06.021, 2011.

~~Bedka, S. T., Minnis, P., Duda, D. P., Chee, T. L., and Palikonda, R.: Properties of linear contrails in the Northern Hemisphere derived from 2006 Aqua MODIS observations, Geophysical Research Letters, 40, 772-777, https://doi.org/10.1029/2012GL054363, 2013.~~

Biele, J., Beyerle, G., and Baumgarten, G.: Polarization lidar: Corrections of instrumental effects, Opt. Express, 7, 427-435, 10.1364/OE.7.000427, 2000.

Bier, A., Burkhardt, U., and Bock, L.: Synoptic Control of Contrail Cirrus Life Cycles and Their Modification Due to Reduced Soot Number Emissions, Journal of Geophysical Research: Atmospheres, 122, 11,584-511,603, https://doi.org/10.1002/2017JD027011, 2017.

Bock, L. and Burkhardt, U.: The temporal evolution of a long-lived contrail cirrus cluster: Simulations with a global climate model, Journal of Geophysical Research: Atmospheres, 121, 3548-3565, https://doi.org/10.1002/2015JD024475, 2016.

Bräuer, T., Voigt, C., Sauer, D., Kaufmann, S., Hahn, V., Scheibe, M., Schlager, H., Huber, F., Le Clercq, P., Moore, R. H., and Anderson, B. E.: Reduced ice number concentrations in contrails from low-aromatic biofuel blends, Atmos. Chem. Phys., 21, 16817-16826, 10.5194/acp-21-16817-2021, 2021a.

Bräuer, T., Voigt, C., Sauer, D., Kaufmann, S., Hahn, V., Scheibe, M., Schlager, H., Diskin, G. S., Nowak, J. B., DiGangi, J. P., Huber, F., Moore, R. H., and Anderson, B. E.: Airborne Measurements of Contrail Ice Properties - Dependence on Temperature and Humidity, Geophysical Research Letters, 48, e2020GL092166, https://doi.org/10.1029/2020GL092166, 2021b.

Braga, R. C., Rosenfeld, D., Weigel, R., Jurkat, T., Andreae, M. O., Wendisch, M., Pöhlker, M. L., Klimach, T., Pöschl, U., Pöhlker, C., Voigt, C., Mahnke, C., Borrmann, S., Albrecht, R. I., Molleker, S., Vila, D. A., Machado, L. A. T., and Artaxo, P.: Comparing parameterized versus measured microphysical properties of tropical convective cloud bases during the ACRIDICON–CHUVA campaign, Atmos. Chem. Phys., 17, 7365–7386, https://doi.org/10.5194/acp-17-7365-2017, 2017a.

Braga, R. C., Rosenfeld, D., Weigel, R., Jurkat, T., Andreae, M. O., Wendisch, M., Pöschl, U., Voigt, C., Mahnke, C., Borrmann, S., Albrecht, R. I., Molleker, S., Vila, D. A., Machado, L. A. T., and Grulich, L.: Further evidence for CCN aerosol concentrations determining the height of warm rain and ice initiation in convective clouds over the Amazon basin, Atmos. Chem. Phys., 17, 14433–14456, https://doi.org/10.5194/acp-17-14433-2017, 2017b.

Buehler, S. A., John, V. O., Kottayil, A., Milz, M., and Eriksson, P.: Efficient radiative transfer simulations for a broadband infrared radiometer-Combining a weighted mean of representative frequencies approach with frequency selection by simulated annealing, Journal of Quantitative Spectroscopy and Radiative Transfer, 111, 602-615, https://doi.org/10.1016/j.jqsrt.2009.10.018, 2010.

Bugliaro, L., Zinner, T., Keil, C., Mayer, B., Hollmann, R., Reuter, M., and Thomas, W.: Validation of cloud property retrievals with simulated satellite radiances: a case study for SEVIRI, Atmos. Chem. Phys., 11, 5603-5624, 10.5194/acp-11-5603-2011, 2011.

Bugliaro, L., Piontek, D., Kox, S., Schmidl, M., Mayer, B., Müller, R., Vázquez-Navarro, M., Peters, D. M., Grainger, R. G., Gasteiger, J., and Kar, J.: VADUGS: a neural network for the remote sensing of volcanic ash with MSG/SEVIRI trained with synthetic thermal satellite observations simulated with a radiative transfer model, Nat. Hazards Earth Syst. Sci., 22, 1029–1054, https://doi.org/10.5194/nhess-22-1029-2022, 2022.

~~Burkhardt, U. and Kärcher, B.: Process-based simulation of contrail cirrus in a global climate model, Journal of Geophysical Research: Atmospheres, 114, https://doi.org/10.1029/2008JD011491, 2009.~~

Burkhardt, U. and Kärcher, B.: Global radiative forcing from contrail cirrus, Nature Climate Change, 1, 54-58, 10.1038/nclimate1068, 2011.

Burkhardt, U., Bock, L., and Bier, A.: Mitigating the contrail cirrus climate impact by reducing aircraft soot number emissions, npj Climate and Atmospheric Science, 1, 37, 10.1038/s41612-018-0046-4, 2018.

Chauvigné, A., Jourdan, O., Schwarzenboeck, A., Gourbeyre, C., Gayet, J. F., Voigt, C., Schlager, H., Kaufmann, S., Borrmann, S., Molleker, S., Minikin, A., Jurkat, T., and Schumann, U.: Statistical analysis of contrail to cirrus evolution during the Contrail and Cirrus Experiment (CONCERT), Atmos. Chem. Phys., 18, 9803-9822, 10.5194/acp-18-9803-2018, 2018.

Chen, C.-C., Gettelman, A., Craig, C., Minnis, P., and Duda, D. P.: Global contrail coverage simulated by CAM5 with the inventory of 2006 global aircraft emissions, Journal of Advances in Modeling Earth Systems, 4, https://doi.org/10.1029/2011MS000105, 2012.

~~Clerbaux, N., Russell, J. E., Dewitte, S., Bertrand, C., Caprion, D., De Paepe, B., Gonzalez Sotelino, L., Ipe, A., Bantges, R., and Brindley, H. E.: Comparison of GERB instantaneous radiance and flux products with CERES Edition 2 data, Remote Sensing of Environment, 113, 102-114, https://doi.org/10.1016/j.rse.2008.08.016, 2009.~~

Cox, C. and Munk, W.: Measurement of the roughness of the sea surface from photographs of the sun's glitter, J. Opt. Soc. USA, 44, 838–850, 1954a.

Cox, C. and Munk, W.: Statistics of the sea surface derived from sun glitter, J. Marine Res., 13, 198–227, 1954b.

de Reus, M., Borrmann, S., Bansemer, A., Heymsfield, A. J., Weigel, R., Schiller, C., Mitev, V., Frey, W., Kunkel, D., Kürten, A., Curtius, J., Sitnikov, N. M., Ulanovsky, A., and Ravegnani, F.: Evidence for ice particles in the tropical stratosphere from in-situ measurements, Atmos. Chem. Phys., 9, 6775-6792, 10.5194/acp-9-6775-2009, 2009.

Duda, D. P., Minnis, P., and Nguyen, L.: Estimates of cloud radiative forcing in contrail clusters using GOES imagery, Journal of Geophysical Research: Atmospheres, 106, 4927-4937, https://doi.org/10.1029/2000JD900393, 2001.

Duda, D. P., Minnis, P., Nguyen, L., and Palikonda, R.: A Case Study of the Development of Contrail Clusters over the Great Lakes, Journal of the Atmospheric Sciences, 61, 1132-1146, 10.1175/1520-0469(2004)061<1132:ACSOTD>2.0.CO;2, 2004.

Duda, D. P., Minnis, P., Khlopenkov, K., Chee, T. L., and Boeke, R.: Estimation of 2006 Northern Hemisphere contrail coverage using MODIS data, Geophysical Research Letters, 40, 612-617, https://doi.org/10.1002/grl.50097, 2013.

Emde, C., Buras-Schnell, R., Kylling, A., Mayer, B., Gasteiger, J., Hamann, U., Kylling, J., Richter, B., Pause, C., Dowling, T., and Bugliaro, L.: The libRadtran software package for radiative transfer calculations (version 2.0.1), Geosci. Model Dev., 9, 1647–1672, https://doi.org/10.5194/gmd-9-1647-2016, 2016.

Esselborn, M., Wirth, M., Fix, A., Tesche, M., and Ehret, G.: Airborne high spectral resolution lidar for measuring aerosol extinction and backscatter coefficients, Applied Optics, 47, 346–358, 2008.

Fischler, M. A. and Bolles, R. C.: Random Sample Consensus: A Paradigm for Model Fitting with Applications to Image Analysis and Automated Cartography. Comm. ACM. 24: 381–395. doi:10.1145/358669.358692, 1981.

Forster, P., Ramaswamy, V., Artaxo, P., Berntsen, T., Betts, R., Fahey, D. W., Haywood, J., Lean, J., Lowe, D. C., Myhre, G., Nganga, J., Prinn, R., Raga, G., Schulz, M., and Van Dorland, R.: Changes in Atmospheric Constituents and in Radiative Forcing. Cambridge University Press, Cambridge, United Kingdom and New York, NY, USA, 2007.

Gasteiger, J., Emde, C., Mayer, B., Buras, R., Buehler, S.A. and Lemke, O.: Representative wavelengths absorption parameterization applied to satellite channels and spectral bands, Journal of Quantitative Spectroscopy and Radiative Transfer, 148, 99-115, https://doi.org/10.1016/j.jqsrt.2014.06.024, 2014.

Gayet, J. F., Shcherbakov, V., Voigt, C., Schumann, U., Schäuble, D., Jessberger, P., Petzold, A., Minikin, A., Schlager, H., Dubovik, O., and Lapyonok, T.: The evolution of microphysical and optical properties of an A380 contrail in the vortex phase, Atmos. Chem. Phys., 12, 6629-6643, https://doi.org/10.5194/acp-12-6629-2012, 2012.

~~Gettelman, A. and Chen, C.: The climate impact of aviation aerosols, Geophysical Research Letters, 40, 2785-2789, https://doi.org/10.1002/grl.50520, 2013.~~

Gettelman, A., Chen, C. C., and Bardeen, C. G.: The climate impact of COVID-19-induced contrail changes, Atmos. Chem. Phys., 21, 9405-9416, 10.5194/acp-21-9405-2021, 2021.

Gierens, K., Matthes, S., and Rohs, S.: How Well Can Persistent Contrails Be Predicted?, Aerospace, 7, 10.3390/aerospace7120169, 2020.

Graf, K., Schumann, U., Mannstein, H., and Mayer, B.: Aviation induced diurnal North Atlantic cirrus cover cycle, Geophysical Research Letters, 39, https://doi.org/10.1029/2012GL052590, 2012.

Grewe, V., Dahlmann, K., Flink, J., Frömming, C., Ghosh, R., Gierens, K., Heller, R., Hendricks, J., Jöckel, P., Kaufmann, S., Kölker, K., Linke, F., Luchkova, T., Lührs, B., Van Manen, J., Matthes, S., Minikin, A., Niklaß, M., Plohr, M., Righi, M., Rosanka, S., Schmitt, A., Schumann, U., Terekhov, I., Unterstrasser, S., Vázquez-Navarro, M., Voigt, C., Wicke, K., Yamashita, H., Zahn, A., and Ziereis, H.: Mitigating the Climate Impact from Aviation: Achievements and Results of the DLR WeCare Project, Aerospace, 4, 10.3390/aerospace4030034, 2017.

Groß, S., Wirth, M., Schäfler, A., Fix, A., Kaufmann, S., and Voigt, C.: Potential of airborne lidar measurements for cirrus cloud studies, 7, 2745–2755, https://doi.org/10.5194/amt-7-2745-2014, 2014.

Harries, J. E., Russell, J. E., Hanafin, J. A., Brindley, H., Futyan, J., Rufus, J., Kellock, S., Matthews, G., Wrigley, R., Last, A., Mueller, J., Mossavati, R., Ashmall, J., Sawyer, E., Parker, D., Caldwell, M., Allan, P. M., Smith, A., Bates, M. J., Coan, B., Stewart, B. C., Lepine, D. R., Cornwall, L. A., Corney, D. R., Ricketts, M. J., Drummond, D., Smart, D., Cutler, R., Dewitte, S., Clerbaux, N., Gonzalez, L., Ipe, A., Bertrand, C., Joukoff, A., Crommelynck, D., Nelms, N., Llewellyn-Jones, D. T., Butcher, G., Smith, G. L., Szewczyk, Z. P., Mlynczak, P. E., Slingo, A., Allan, R. P., and Ringer, M. A.: The Geostationary Earth Radiation Budget Project, Bulletin of the American Meteorological Society, 86, 945-960, 10.1175/BAMS-86-7-945, 2005.

Haywood, J. M., Allan, R. P., Bornemann, J., Forster, P. M., Francis, P. N., Milton, S., Rädel, G., Rap, A., Shine, K. P., and Thorpe, R.: A case study of the radiative forcing of persistent contrails evolving into contrail-induced cirrus, Journal of Geophysical Research: Atmospheres, 114, https://doi.org/10.1029/2009JD012650, 2009.

Hendricks, J., Kärcher, B., Lohmann, U., and Ponater, M.: Do aircraft black carbon emissions affect cirrus clouds on the global scale?, Geophysical Research Letters, 32, https://doi.org/10.1029/2005GL022740, 2005.

Hersbach, H., Bell, B., Berrisford, P., Hirahara, S., Horányi, A., Muñoz-Sabater, J., Nicolas, J., Peubey, C., Radu, R., Schepers, D., Simmons, A., Soci, C., Abdalla, S., Abellan, X., Balsamo, G., Bechtold, P., Biavati, G., Bidlot, J., Bonavita, M., De Chiara, G., Dahlgren, P., Dee, D., Diamantakis, M., Dragani, R., Flemming, J., Forbes, R., Fuentes, M., Geer, A., Haimberger, L., Healy, S., Hogan, R. J., Hólm, E., Janisková, M., Keeley, S., Laloyaux, P., Lopez, P., Lupu, C., Radnoti, G., de Rosnay, P., Rozum, I., Vamborg, F., Villaume, S., and Thépaut, J.-N.: The ERA5 global reanalysis, Quarterly Journal of the Royal Meteorological Society, 146, 1999-2049, https://doi.org/10.1002/qj.3803, 2020.

Heymsfield, A., Baumgardner, D., DeMott, P., Forster, P., Gierens, K., and Kärcher, B.: Contrail Microphysics, Bulletin of the American Meteorological Society, 91, 465-472, 10.1175/2009BAMS2839.1, 2010a.

Heymsfield, A. J., Kennedy, P. C., Massie, S., Schmitt, C., Wang, Z., Haimov, S., and Rangno, A.: Aircraft-Induced Hole Punch and Canal Clouds: Inadvertent Cloud Seeding, Bulletin of the American Meteorological Society, 91, 753-766, 10.1175/2009BAMS2905.1, 2010b.

~~Iwabuchi, H., Yang, P., Liou, K. N., and Minnis, P.: Physical and optical properties of persistent contrails: Climatology and interpretation, Journal of Geophysical Research: Atmospheres, 117, https://doi.org/10.1029/2011JD017020, 2012.~~

Järvinen, E., Schnaiter, M., Mioche, G., Jourdan, O., Shcherbakov, V. N., Costa, A., Afchine, A., Krämer, M., Heidelberg, F., Jurkat, T., Voigt, C., Schlager, H., Nichman, L., Gallagher, M., Hirst, E., Schmitt, C., Bansemer, A., Heymsfield, A., Lawson, P., Tricoli, U., Pfeilsticker, K., Vochezer, P., Möhler, O., and Leisner, T.: Quasi-Spherical Ice in Convective Clouds, Journal of the Atmospheric Sciences, 73, 3885-3910, 10.1175/JAS-D-15-0365.1, 2016.

Jensen, E. J., Ackerman, A. S., Stevens, D. E., Toon, O. B., and Minnis, P.: Spreading and growth of contrails in a sheared environment, Journal of Geophysical Research: Atmospheres, 103, 31557-31567, https://doi.org/10.1029/98JD02594, 1998a.

Jensen, E. J., Toon, O. B., Kinne, S., Sachse, G. W., Anderson, B. E., Chan, K. R., Twohy, C. H., Gandrud, B., Heymsfield, A., and Miake-Lye, R. C.: Environmental conditions required for contrail formation and persistence, Journal of Geophysical Research: Atmospheres, 103, 3929-3936, https://doi.org/10.1029/97JD02808, 1998b.

Jeßberger, P., Voigt, C., Schumann, U., Sölch, I., Schlager, H., Kaufmann, S., Petzold, A., Schäuble, D., and Gayet, J. F.: Aircraft type influence on contrail properties, Atmos. Chem. Phys., 13, 11965-11984, 10.5194/acp-13-11965-2013, 2013.

Jurkat, T., Voigt, C., Arnold, F., Schlager, H., Kleffmann, J., Aufmhoff, H., Schäuble, D., Schaefer, M., and Schumann, U.: Measurements of HONO, NO, NOy and SO2 in aircraft exhaust plumes at cruise, Geophysical Research Letters, 38, https://doi.org/10.1029/2011GL046884, 2011.

Jurkat, T., Kaufmann, S., Voigt, C., Schäuble, D., Jeßberger, P., and Ziereis, H.: The airborne mass spectrometer AIMS – Part 2: Measurements of trace gases with stratospheric or tropospheric origin in the UTLS, Atmos. Meas. Tech., 9, 1907–1923, https://doi.org/10.5194/amt-9-1907-2016, 2016.

Kärcher, B. and Voigt, C.: Susceptibility of contrail ice crystal numbers to aircraft soot particle emissions, Geophysical Research Letters, 44, 8037-8046, https://doi.org/10.1002/2017GL074949, 2017. ~~Kärcher, B., Burkhardt, U., Bier, A., Bock, L., and Ford, I. J.: The microphysical pathway to contrail formation, Journal of Geophysical Research: Atmospheres, 120, 7893-7927, https://doi.org/10.1002/2015JD023491, 2015.~~

Kärcher, B.: Formation and radiative forcing of contrail cirrus, Nature Communications, 9, 1824, 10.1038/s41467-018-04068-0, 2018.

~~Kärcher, B., Kleine, J., Sauer, D., and Voigt, C.: Contrail Formation: Analysis of Sublimation Mechanisms, Geophysical Research Letters, 45, 13,547-513,552, https://doi.org/10.1029/2018GL079391, 2018.~~

~~Kärcher, B., Mahrt, F., and Marcolli, C.: Process-oriented analysis of aircraft soot-cirrus interactions constrains the climate impact of aviation, Communications Earth & Environment, 2, 113, 10.1038/s43247-021-00175-x, 2021.~~

Kaufmann, S., Voigt, C., Jurkat, T., Thornberry, T., Fahey, D. W., Gao, R. S., Schlage, R., Schäuble, D., and Zöger, M.: The airborne mass spectrometer AIMS – Part 1: AIMS-H2O for UTLS water vapor measurements, Atmos. Meas. Tech., 9, 939-953, 10.5194/amt-9-939-2016, 2016.

Kaufmann, S., Voigt, C., Heller, R., Jurkat-Witschas, T., Krämer, M., Rolf, C., Zöger, M., Giez, A., Buchholz, B., Ebert, V., Thornberry, T., and Schumann, U.: Intercomparison of midlatitude tropospheric and lower-stratospheric water vapor measurements and comparison to ECMWF humidity data, Atmos. Chem. Phys., 18, 16729-16745, 10.5194/acp-18-16729-2018, 2018.

Kiemle, C., Wirth, M., Fix, A., Ehret, G., Schumann, U., Gardiner, T., Schiller, C., Sitnikov, N., and Stiller, G.: First airborne water vapor lidar measurements in the tropical upper troposphere and mid-latitudes lower stratosphere: accuracy evaluation and intercomparisons with other instruments, 8, 5245-5261, https://doi.org/10.5194/acp-8-5245-2008, 2008.

Kleine, J., Voigt, C., Sauer, D., Schlager, H., Scheibe, M., Jurkat-Witschas, T., Kaufmann, S., Kärcher, B., and Anderson, B. E.: In Situ Observations of Ice Particle Losses in a Young Persistent Contrail, Geophysical Research Letters, 45, 13,553-513,561, https://doi.org/10.1029/2018GL079390, 2018.

Krautstrunk M., and Giez A.: The Transition from FALCON to HALO Era Airborne Atmospheric Research. In: Schumann U. (eds) Atmospheric Physics. Research Topics in Aerospace. Springer, Berlin, Heidelberg, 2012.

Kübbeler, M., Hildebrandt, M., Meyer, J., Schiller, C., Hamburger, Th., Jurkat, T., Minikin, A., Petzold, A., Rautenhaus, M., Schlager, H., Schumann, U., Voigt, C., Spichtinger, P., Gayet, J.-F., Gourbeyre, C., and Krämer, M.: Thin and subvisible cirrus and contrails in a subsaturated environment, Atmos. Chem. Phys., 11, 5853–5865, https://doi.org/10.5194/acp-11-5853-2011, 2011.

~~Lee, D. S., Fahey, D. W., Forster, P. M., Newton, P. J., Wit, R. C. N., Lim, L. L., Owen, B., and Sausen, R.: Aviation and global climate change in the 21st century, Atmospheric Environment, 43, 3520-3537, https://doi.org/10.1016/j.atmosenv.2009.04.024, 2009.~~

Lee, D. S., Fahey, D. W., Skowron, A., Allen, M. R., Burkhardt, U., Chen, Q., Doherty, S. J., Freeman, S., Forster, P. M., Fuglestvedt, J., Gettelman, A., De León, R. R., Lim, L. L., Lund, M. T., Millar, R. J., Owen, B., Penner, J. E., Pitari, G., Prather, M. J., Sausen, R., and Wilcox, L. J.: The contribution of global aviation to anthropogenic climate forcing for 2000 to 2018, Atmospheric Environment, 244, 117834, https://doi.org/10.1016/j.atmosenv.2020.117834, 2021.

Letu, H., Ishimoto, H., Riedi, J., Nakajima, T. Y., C.-Labonnote, L., Baran, A. J., Nagao, T. M., and Sekiguchi, M.: Investigation of ice particle habits to be used for ice cloud remote sensing for the GCOM-C satellite mission, Atmos. Chem. Phys., 16, 12287–12303, https://doi.org/10.5194/acp-16-12287-2016, 2016.

Li, Q. and Groß, S.: Changes in cirrus cloud properties and occurrence over Europe during the COVID-19-caused air traffic reduction, Atmos. Chem. Phys., 21, 14573-14590, 10.5194/acp-21-14573-2021, 2021.

Mannstein, H., Brömser, A., and Bugliaro, L.: Ground-based observations for the validation of contrails and cirrus detection in satellite imagery, Atmos. Meas. Tech., 3, 655–669, https://doi.org/10.5194/amt-3-655-2010, 2010.

Marjani, S., Tesche, M., Bräuer, P., Sourdeval, O., and Quaas, J.: Satellite Observations of the Impact of Individual Aircraft on Ice Crystal Number in Thin Cirrus Clouds, Geophysical Research Letters, 49, e2021GL096173, https://doi.org/10.1029/2021GL096173, 2022.

Mayer, B. and Kylling, A.: Technical note: The libRadtran software package for radiative transfer calculations - description and examples of use, Atmos. Chem. Phys., 5, 1855-1877, 10.5194/acp-5-1855-2005, 2005.

Meijer, V. R., Kulik, L., Eastham, S. D., Allroggen, F., Speth, R. L., Karaman, S., and Barrett, S. R. H.: Contrail coverage over the United States before and during the COVID-19 pandemic, Environmental Research Letters, 17, 034039, 10.1088/1748-9326/ac26f0, 2022.

Minnis, P., Ayers, J. K., Palikonda, R., and Phan, D.: Contrails, Cirrus Trends, and Climate, Journal of Climate, 17, 1671-1685, 10.1175/1520-0442(2004)017<1671:CCTAC>2.0.CO;2, 2004.

Minnis, P., Bedka, S. T., Duda, D. P., Bedka, K. M., Chee, T., Ayers, J. K., Palikonda, R., Spangenberg, D. A., Khlopenkov, K. V., and Boeke, R.: Linear contrail and contrail cirrus properties determined from satellite data, Geophysical Research Letters, 40, 3220-3226, https://doi.org/10.1002/grl.50569, 2013.

~~Muhlbauer, A., Ackerman, T. P., Comstock, J. M., Diskin, G. S., Evans, S. M., Lawson, R. P., and Marchand, R. T.: Impact of large scale dynamics on the microphysical properties of midlatitude cirrus, J. Geophys. Res. Atmos., 119, 3976–3996, http://doi.org/10.1002/2013JD020035, 2014.~~Nakajima, T. and Tanaka, M.: Effect of wind-generated waves on the transfer of solar radiation in the atmosphere-ocean system, Journal of Quantitative Spectroscopy and Radiative Transfer, 29, 521-537, https://doi.org/10.1016/0022-4073(83)90129-2, 1983.

Petzold, A., Busen, R., Schröder, F. P., Baumann, R., Kuhn, M., Ström, J., Hagen, D. E., Whitefield, P. D., Baumgardner, D., Arnold, F., Borrmann, S., and Schumann, U.: Near-field measurements on contrail properties from fuels with different sulfur content, Journal of Geophysical Research: Atmospheres, 102, 29867-29880, https://doi.org/10.1029/97JD02209, 1997.

Quaas, J., Gryspeerdt, E., Vautard, R., and Boucher, O.: Climate impact of aircraft-induced cirrus assessed from satellite observations before and during COVID-19, Environmental Research Letters, 16, 064051, 10.1088/1748-9326/abf686, 2021.

Rädel, G. and Shine, K. P.: Radiative forcing by persistent contrails and its dependence on cruise altitudes, Journal of Geophysical Research: Atmospheres, 113, https://doi.org/10.1029/2007JD009117, 2008.

~~Righi, M., Hendricks, J., and Beer, C. G.: Exploring the uncertainties in the aviation soot–cirrus effect, Atmos. Chem. Phys., 21, 17267–17289, 10.5194/acp-21-17267-2021, 2021.~~

Rodríguez De León, R., Lim, L. L., Lee, D. S., Bennett, M., and Krämer, M.: Simple Versus Complex Physical Representation of the Radiative Forcing From Linear Contrails: A Sensitivity Analysis, Journal of Geophysical Research: Atmospheres, 123, 2831-2840, https://doi.org/10.1002/2017JD027861, 2018.

Sanz-Morère, I., Eastham, S. D., Speth, R. L., and Barrett, S. R. H.: Reducing Uncertainty in Contrail Radiative Forcing Resulting from Uncertainty in Ice Crystal Properties, Environmental Science & Technology Letters, 7, 371-375, 10.1021/acs.estlett.0c00150, 2020.

Sanz-Morère, I., Eastham, S. D., Allroggen, F., Speth, R. L., and Barrett, S. R. H.: Impacts of multi-layer overlap on contrail radiative forcing, Atmos. Chem. Phys., 21, 1649–1681, https://doi.org/10.5194/acp-21-1649-2021, 2021.

Schlager, H., P. Konopka, P. Schulte, U. Schumann, H. Ziereis, F. Arnold, M. Klemm, D.E. Hagen, P.D. Whitefield, and J. Ovarlez, In situ observations of airtraffic emission signatures in the North Atlantic Flight Corridor, Journal of Geophysical Research: Atmospheres, 102, 10739-10750, https://doi.org/10.1029/96JD03748, 1997

Schmetz, J., Pili, P., Tjemkes, S., Just, D., Kerkmann, J., Rota, S., and Ratier, A.: AN INTRODUCTION TO METEOSAT SECOND GENERATION (MSG), Bulletin of the American Meteorological Society, 83, 977-992, 10.1175/1520-0477(2002)083<0977:AITMSG>2.3.CO;2, 2002.

Schröder, F., Brock, C. A., Baumann, R., Petzold, A., Busen, R., Schulte, P., and Fiebig, M.: In situ studies on volatile jet exhaust particle emissions: Impact of fuel sulfur content and environmental conditions on nuclei mode aerosols, Journal of Geophysical Research: Atmospheres, 105, 19941-19954, https://doi.org/10.1029/2000JD900112, 2000.

Schumann, U.: On conditions for contrail formation from aircraft exhausts, Meteorologische Zeitschrift, 5, 4–23, 10.1127/metz/5/1996/4, 1996.

Schumann, U., Schlager, H., Arnold, F., Baumann, R., Haschberger, P., and Klemm, O.: Dilution of aircraft exhaust plumes at cruise altitudes, Atmospheric Environment, 32, 3097-3103, https://doi.org/10.1016/S1352-2310(97)00455-X, 1998.

Schumann, U., Jeßberger, P., and Voigt, C.: Contrail ice particles in aircraft wakes and their climatic importance, Geophysical Research Letters, 40, 2867-2872, https://doi.org/10.1002/grl.50539, 2013.

Schumann, U. and Graf, K.: Aviation-induced cirrus and radiation changes at diurnal timescales, Journal of Geophysical Research: Atmospheres, 118, 2404-2421, https://doi.org/10.1002/jgrd.50184, 2013.

~~Schumann, U., Penner, J. E., Chen, Y., Zhou, C., and Graf, K.: Dehydration effects from contrails in a coupled contrail–climate model, Atmos. Chem. Phys., 15, 11179-11199, 10.5194/acp-15-11179-2015, 2015.~~

Schumann, U., Baumann, R., Baumgardner, D., Bedka, S. T., Duda, D. P., Freudenthaler, V., Gayet, J. F., Heymsfield, A. J., Minnis, P., Quante, M., Raschke, E., Schlager, H., Vázquez-Navarro, M., Voigt, C., and Wang, Z.: Properties of individual contrails: a compilation of observations and some comparisons, Atmos. Chem. Phys., 17, 403-438, 10.5194/acp-17-403-2017, 2017.

Schumann, U., Bugliaro, L., Dörnbrack, A., Baumann, R., and Voigt, C.: Aviation Contrail Cirrus and Radiative Forcing Over Europe During 6 Months of COVID-19, Geophysical Research Letters, 48, e2021GL092771, https://doi.org/10.1029/2021GL092771, 2021a.

Schumann, U., Poll, I., Teoh, R., Koelle, R., Spinielli, E., Molloy, J., Koudis, G. S., Baumann, R., Bugliaro, L., Stettler, M., and Voigt, C.: Air traffic and contrail changes over Europe during COVID-19: a model study, Atmos. Chem. Phys., 21, 7429-7450, 10.5194/acp-21-7429-2021, 2021b.

Stamnes, K., Tsay, S.-C., and Laszlo, I.: DISORT, A General Purpose Fortran Program for Discrete-Ordinate-Method Radiative Transfer in Scattering and Emitting Layered Media: Documentation and Methodology, Tech. rep., Stevens Insitute of Technology, Hoboken, NJ, USA, 2000.

Stordal, F., Myhre, G., Stordal, E. J. G., Rossow, W. B., Lee, D. S., Arlander, D. W., and Svendby, T.: Is there a trend in cirrus cloud cover due to aircraft traffic? Atmos. Chem. Phys., 5, 2155-2162, 10.5194/acp-5-2155-2005, 2005.

Strandgren, J., Bugliaro, L., Sehnke, F., and Schröder, L.: Cirrus cloud retrieval with MSG/SEVIRI using artificial neural networks, Atmos. Meas. Tech., 10, 3547-3573, 10.5194/amt-10-3547-2017, 2017a.

Strandgren, J., Fricker, J., and Bugliaro, L.: Characterisation of the artificial neural network CiPS for cirrus cloud remote sensing with MSG/SEVIRI, Atmos. Meas. Tech., 10, 4317–4339, https://doi.org/10.5194/amt-10-4317-2017, 2017b.

Stratmann, G., Ziereis, H., Stock, P., Brenninkmeijer, C. A. M., Zahn, A., Rauthe-Schöch, A., Velthoven, P. V., Schlager, H., and Volz-Thomas, A.: NO and NOy in the upper troposphere: Nine years of CARIBIC measurements onboard a passenger aircraft, Atmospheric Environment, 133, 93-111, https://doi.org/10.1016/j.atmosenv.2016.02.035, 2016.

Stuber, N., Forster, P., Rädel, G., and Shine, K.: The importance of the diurnal and annual cycle of air traffic for contrail radiative forcing, Nature, 441, 864-867, 10.1038/nature04877, 2006.

Teoh, R., Schumann, U., Gryspeerdt, E., Shapiro, M., Molloy, J., Koudis, G., Voigt, C., and Stettler, M. E. J.: Aviation contrail climate effects in the North Atlantic from 2016 to 2021, Atmos. Chem. Phys., 22, 10919–10935, https://doi.org/10.5194/acp-22-10919-2022, 2022a.

Teoh, R., Schumann, U., Voigt, C., Schripp, T., Shapiro, M., Engberg, Z., Molloy, J., Koudis, G., and Stettler, M. E. J.: Targeted Use of Sustainable Aviation Fuel to Maximize Climate Benefits, Environmental Science & Technology, 10.1021/acs.est.2c05781, 2022b.

Tesche, M., Achtert, P., Glantz, P., and Noone, K. J.: Aviation effects on already-existing cirrus clouds, Nature Communications, 7, 12016, 10.1038/ncomms12016, 2016.

~~Unterstrasser, S. and Gierens, K.: Numerical simulations of contrail-to-cirrus transition – Part 1: An extensive parametric study, Atmos. Chem. Phys., 10, 2017–2036, https://doi.org/10.5194/acp-10-2017-2010, 2010.~~

Unterstrasser, S., Gierens, K., Sölch, I., and Lainer, M.: Numerical simulations of homogeneously nucleated natural cirrus and contrail-cirrus. Part 1: How different are they?, Meteorologische Zeitschrift, 26, 621-642, https://doi.org/10.1127/metz/2016/0777, 2017a.

Unterstrasser, S., Gierens, K., Sölch, I., and Wirth, M.: Numerical simulations of homogeneously nucleated natural cirrus and contrail-cirrus. Part 2: Interaction on local scale, Meteorologische Zeitschrift, 26, 643-661, http://dx.doi.org/10.1127/metz/2016/0780, 2017b.

Urbanek, B., Groß, S., Wirth, M., Rolf, C., Krämer, M., and Voigt, C.: High Depolarization Ratios of Naturally Occurring Cirrus Clouds Near Air Traffic Regions Over Europe, Geophysical Research Letters, 45, 13,166-113,172, https://doi.org/10.1029/2018GL079345, 2018.

Vázquez-Navarro, M., Mayer, B., and Mannstein, H.: A fast method for the retrieval of integrated longwave and shortwave top-of-atmosphere upwelling irradiances from MSG/SEVIRI (RRUMS), Atmos. Meas. Tech., 6, 2627-2640, 10.5194/amt-6-2627-2013, 2013.

Vázquez-Navarro, M., Mannstein, H., and Kox, S.: Contrail life cycle and properties from 1 year of MSG/SEVIRI rapid-scan images, Atmos. Chem. Phys., 15, 8739–8749, https://doi.org/10.5194/acp-15-8739-2015, 2015.

Verma, P. and Burkhardt, U.: Contrail formation within cirrus: ICON-LEM simulations of the impact of cirrus cloud properties on contrail formation, Atmos. Chem. Phys., 22, 8819–8842, https://doi.org/10.5194/acp-22-8819-2022, 2022.

Voigt, C., Schumann, U., Jurkat, T., Schäuble, D., Schlager, H., Petzold, A., Gayet, J. F., Krämer, M., Schneider, J., Borrmann, S., Schmale, J., Jessberger, P., Hamburger, T., Lichtenstern, M., Scheibe, M., Gourbeyre, C., Meyer, J., Kübbeler, M., Frey, W., Kalesse, H., Butler, T., Lawrence, M. G., Holzäpfel, F., Arnold, F., Wendisch, M., Döpelheuer, A., Gottschaldt, K., Baumann, R., Zöger, M., Sölch, I., Rautenhaus, M., and Dörnbrack, A.: In-situ observations of young contrails – overview and selected results from the CONCERT campaign, Atmos. Chem. Phys., 10, 9039-9056, 10.5194/acp-10-9039-2010, 2010.

Voigt, C., Schumann, U., Jessberger, P., Jurkat, T., Petzold, A., Gayet, J. F., Krämer, M., Thornberry, T., and Fahey, D. W.: Extinction and optical depth of contrails, Geophysical Research Letters, 38, https://doi.org/10.1029/2011GL047189, 2011.

Voigt, C., Schumann, U., Minikin, A., Abdelmonem, A., Afchine, A., Borrmann, S., Boettcher, M., Buchholz, B., Bugliaro, L., Costa, A., Curtius, J., Dollner, M., Dörnbrack, A., Dreiling, V., Ebert, V., Ehrlich, A., Fix, A., Forster, L., Frank, F., Fütterer, D., Giez, A., Graf, K., Grooß, J.-U., Groß, S., Heimerl, K., Heinold, B., Hüneke, T., Järvinen, E., Jurkat, T., Kaufmann, S., Kenntner, M., Klingebiel, M., Klimach, T., Kohl, R., Krämer, M., Krisna, T. C., Luebke, A., Mayer, B., Mertes, S., Molleker, S., Petzold, A., Pfeilsticker, K., Port, M., Rapp, M., Reutter, P., Rolf, C., Rose, D., Sauer, D., Schäfler, A., Schlage, R., Schnaiter, M., Schneider, J., Spelten, N., Spichtinger, P., Stock, P., Walser, A., Weigel, R., Weinzierl, B., Wendisch, M., Werner, F., Wernli, H., Wirth, M., Zahn, A., Ziereis, H., and Zöger, M.: ML-CIRRUS: The Airborne Experiment on Natural Cirrus and Contrail Cirrus with the High-Altitude Long-Range Research Aircraft HALO, Bulletin of the American Meteorological Society, 98, 271-288, 10.1175/BAMS-D-15-00213.1, 2017.

Voigt, C., Kleine, J., Sauer, D., Moore, R. H., Bräuer, T., Le Clercq, P., Kaufmann, S., Scheibe, M., Jurkat-Witschas, T., Aigner, M., Bauder, U., Boose, Y., Borrmann, S., Crosbie, E., Diskin, G. S., DiGangi, J., Hahn, V., Heckl, C., Huber, F., Nowak, J. B., Rapp, M., Rauch, B., Robinson, C., Schripp, T., Shook, M., Winstead, E., Ziemba, L., Schlager, H., and Anderson, B. E.: Cleaner burning aviation fuels can reduce contrail cloudiness, Communications Earth & Environment, 2, 114, 10.1038/s43247-021-00174-y, 2021.

Voigt, C., Lelieveld, J., Schlager, H., Schneider, J., Curtius, J., Meerkötter, R., Sauer, D., Bugliaro, L., Bohn, B., Crowley, J. N., Erbertseder, T., Groβ, S., Hahn, V., Li, Q., Mertens, M., Pöhlker, M. L., Pozzer, A., Schumann, U., Tomsche, L., Williams, J., Zahn, A., Andreae, M., Borrmann, S., Bräuer, T., Dörich, R., Dörnbrack, A., Edtbauer, A., Ernle, L., Fischer, H., Giez, A., Granzin, M., Grewe, V., Harder, H., Heinritzi, M., Holanda, B. A., Jöckel, P., Kaiser, K., Krüger, O. O., Lucke, J., Marsing, A., Martin, A., Matthes, S., Pöhlker, C., Pöschl, U., Reifenberg, S., Ringsdorf, A., Scheibe, M., Tadic, I., Zauner-Wieczorek, M., Henke, R., and Rapp, M.: Cleaner skies during the COVID-19 lockdown, Bulletin of the American Meteorological Society, 10.1175/BAMS-D-21-0012.1, 2022.

Wielicki, B. A., Barkstrom, B. R., Harrison, E. F., Lee, R. B., Smith, G. L., and Cooper, J. E.: Clouds and the Earth's Radiant Energy System (CERES): An Earth Observing System Experiment, Bulletin of the American Meteorological Society, 77, 853-868, 10.1175/1520-0477(1996)077<0853:CATERE>2.0.CO;2, 1996.

Wirth, M., Fix, A., Mahnke, P., Schwarzer, H., Schrandt, F., and Ehret, G.: The airborne multi-wavelength water vapor differential absorption lidar WALES: system design and performance, Applied Physics B: Lasers and Optics, 96, 201–213, 2009.

Yang, P., Hioki, S., Saito, M., Kuo, C.-P., Baum, B. A., and Liou, K.-N.: A Review of Ice Cloud Optical Property Models for Passive Satellite Remote Sensing, Atmosphere, 9, 10.3390/atmos9120499, 2018.

~~Ziereis, H., Schlager, H., Fischer, H., Feigl, C., Hoor, P., Marquardt, R., and Wagner, V.: Aircraft measurements of tracer correlations in the Arctic subvortex region during the Polar Stratospheric Aerosol Experiment (POLSTAR), Journal of Geophysical Research: Atmospheres, 105, 24305-24313, https://doi.org/10.1029/2000JD900288, 2000.~~

Ziereis, H., Hoor, P., Grooß, J.-U., Zahn, A., Stratmann, G., Stock, P., Lichtenstern, M., Krause, J., Bense, V., Afchine, A., Rolf, C., Woiwode, W., Braun, M., Ungermann, J., Marsing, A., Voigt, C., Engel, A., Sinnhuber, B.-M., and Oelhaf, H.: Redistribution of total reactive nitrogen in the lowermost Arctic stratosphere during the cold winter 2015/2016, Atmos. Chem. Phys., 22, 3631–3654, https://doi.org/10.5194/acp-22-3631-2022, 2022.